ATLAS CONF Note

ATLAS-CONF-2018-023

21st June 2018

$E_{\mathrm{T}}^{\mathrm{miss}}$ performance in the ATLAS detector using 2015-2016 LHC pp collisions

The ATLAS Collaboration

The reconstruction and calibration algorithms used to measure missing transverse momentum ($E_{\mathrm{T}}^{\mathrm{miss}}$) with the ATLAS detector utilise energy deposits within the calorimeter and tracks reconstructed in the inner detector and the muon spectrometer. The performance of the $E_{\mathrm{T}}^{\mathrm{miss}}$ reconstruction algorithms is evaluated using data collected in proton–proton collisions in 2015 and 2016 at a centre-of-mass energy of 13 TeV. Results are shown for a data sample corresponding to an integrated luminosity of 36 fb^{-1}. The performance of $E_{\mathrm{T}}^{\mathrm{miss}}$ built with jets reconstructed using a particle flow algorithm is presented and compared to that built with calorimeter jets. Various strategies are used to suppress effects arising from additional proton–proton interactions, called pileup. The tracking and vertexing information is used to distinguish contributions from pileup entering the $E_{\mathrm{T}}^{\mathrm{miss}}$ calculation. The modelling of $E_{\mathrm{T}}^{\mathrm{miss}}$ in simulated events containing a Z boson decaying to two charged leptons (electrons or muons) is compared to data, and estimates of the systematic uncertainties in the $E_{\mathrm{T}}^{\mathrm{miss}}$ measurements are presented.

ATLAS-CONF-2018-023
21 June 2018

© 2018 CERN for the benefit of the ATLAS Collaboration.
Reproduction of this article or parts of it is allowed as specified in the CC-BY-4.0 license.

Contents

1 Introduction

The Large Hadron Collider (LHC) produces proton–proton (pp) collisions at a center-of-mass energy of up to 13 TeV, the by-products of which are measured by the ATLAS detector [1]. Momentum conservation in the plane transverse to the beam axis[1] implies that the transverse momenta of all particles in the final state should sum to effectively zero. Any momentum imbalance may indicate that particles invisible to the detector systems were produced in the collision, such as neutrinos or possibly new particles introduced by physics beyond the Standard Model. This momentum imbalance is known as missing transverse momentum ($E_{\mathrm{T}}^{\mathrm{miss}}$).

The $E_{\mathrm{T}}^{\mathrm{miss}}$ is reconstructed from the signals of all detected particles in the final state, and as such strongly depends on the energy scale and resolution of the reconstructed and calibrated "hard objects": electrons, photons, muons, hadronically decaying τ-leptons, and jets. Reconstructed momentum flow not attributed to any hard objects are reconstructed as the $E_{\mathrm{T}}^{\mathrm{miss}}$ "soft term". Perfectly reconstructed $E_{\mathrm{T}}^{\mathrm{miss}}$ should be equal to the transverse component of the sum of the momenta of invisible particles in the event. However, as $E_{\mathrm{T}}^{\mathrm{miss}}$ is a complicated event-level quality constructed using many different signals in all detector subsystems, it is susceptible to many imperfections. Object momentum mismeasurement, miscalibration, and particles going through un-instrumented regions of the detector all impact $E_{\mathrm{T}}^{\mathrm{miss}}$ reconstruction. Momentum contributions from pileup interactions can enter into the $E_{\mathrm{T}}^{\mathrm{miss}}$ calculation, contaminating the true $E_{\mathrm{T}}^{\mathrm{miss}}$ of the hard scatter interaction of interest. The fake $E_{\mathrm{T}}^{\mathrm{miss}}$ arising from these effects creates distorted distributions compared to true $E_{\mathrm{T}}^{\mathrm{miss}}$ signatures. The performance of $E_{\mathrm{T}}^{\mathrm{miss}}$ reconstruction algorithms is studied with derived quantities such as the mean, the width and the integral of the tail of the $E_{\mathrm{T}}^{\mathrm{miss}}$ distribution.

The $E_{\mathrm{T}}^{\mathrm{miss}}$ reconstructed with different algorithms is studied in both data and Monte Carlo (MC) simulation for different event topologies. Fake $E_{\mathrm{T}}^{\mathrm{miss}}$ is studied using a leptonically decaying Z boson sample which is expected to have no true[2] $E_{\mathrm{T}}^{\mathrm{miss}}$. In MC simulation, the $E_{\mathrm{T}}^{\mathrm{miss}}$ from each algorithm is compared to the true $E_{\mathrm{T}}^{\mathrm{miss}}$, defined as the magnitude of the vector sum of the p_{T} of stable[3] invisible particles from the hard-scatter collision.

The $E_{\mathrm{T}}^{\mathrm{miss}}$ reconstruction algorithms developed by ATLAS for 7 and 8 TeV data from 2010 through 2013 are summarized in Reference [2, 3]. These algorithms were further developed for the 13 TeV data in 2015 and are documented in Reference [4]. This note presents studies evaluating the performance of the $E_{\mathrm{T}}^{\mathrm{miss}}$ reconstruction algorithms in 2015 + 2016 data, and additionally documents the performance of $E_{\mathrm{T}}^{\mathrm{miss}}$ built with Particle Flow jets [5], new techniques for reducing the $E_{\mathrm{T}}^{\mathrm{miss}}$ resolution dependence on pileup, improved strategies for resolving jet and electron or photon energy deposits, and a new strategy for rejecting fake jets arising from calorimeter noise.

This document is organised as follows: Section 2 describes the systems forming the ATLAS detector. Sections 3 and 4 describe the samples and event selections used in the various studies. Sections 5, 6, and 7 give an overview of the $E_{\mathrm{T}}^{\mathrm{miss}}$ definitions and reconstruction strategies.

[1] ATLAS uses a right-handed coordinate system with origin at the nominal interaction point (IP) in the center of the detector and the z-axis along the beam pipe. The x-axis points from the IP to the center of the LHC ring, and the y-axis points upwards. Cylindrical coordinates (r, ϕ) are used in the transverse plane, ϕ being the azimuthal angle around the beam pipe. The pseudorapidity is defined in terms of the polar angle θ as $\eta = -\ln\tan(\theta/2)$.

[2] Some true $E_{\mathrm{T}}^{\mathrm{miss}}$ does arise from neutrinos produced in heavy flavour decays; however, this effect is very small compared to the true $E_{\mathrm{T}}^{\mathrm{miss}}$ in $ZZ \to \ell\ell\nu\nu$ events.

[3] ATLAS defines stable particles as those with an expected laboratory lifetime τ corresponding to $c\tau > 10$ mm.

The event cleaning strategy is documented in Section 8, and the jet selections used in the $E_{\mathrm{T}}^{\mathrm{miss}}$ reconstruction are discussed in Section 9. Section 10 discusses methods used to determine systematic uncertainties associated with the $E_{\mathrm{T}}^{\mathrm{miss}}$ measurement. Section 11 presents the resulting $E_{\mathrm{T}}^{\mathrm{miss}}$ performance.

The summary and outlook are in Section 12.

2 ATLAS detector

The ATLAS experiment [1] is a multipurpose particle physics detector with a forward-backward symmetric cylindrical geometry. It covers almost the whole solid angle around the collision point with layers of tracking detectors (up to $|\eta| = 2.5$), calorimeters (up to $|\eta| = 4.9$), and muon chambers (up to $|\eta| = 2.7$).

The inner detector (ID) is used to reconstruct tracks from the passage of charged particles. The ID has complete azimuthal coverage and spans the region $|\eta| < 2.5$. It consists of layers of high-granularity silicon pixel detectors and silicon microstrip detectors (SCT). A transition radiation tracking detector (TRT) provides coverage for $|\eta| < 2.0$ for additional tracking and particle identification. During the LHC shutdown between Run-1 and Run-2 the Insertable B-Layer (IBL) [6] was added between the previous innermost pixel layer and the beam pipe. A solenoid magnet provides a uniform magnetic field of 2 T inside the tracking detectors, generating track curvature which can be used to determine charged particle momenta.

High granularity liquid-argon (LAr) electromagnetic sampling calorimeters cover the pseudorapidity range $|\eta| < 3.2$. The regions $|\eta| < 1.37$ and $1.5 < |\eta| < 1.8$ feature thin LAr pre-samplers in front the electromagnetic calorimeter. The hadronic calorimetry in the range $|\eta| < 1.7$ is provided by a scintillator-tile calorimeter (Tile), which is separated into a central barrel and two smaller extended barrel cylinders, one on either side of the central barrel. In the end-caps ($|\eta| > 1.5$), the LAr technology is also used for the hadronic calorimeters (HEC), matching the outer $|\eta|$ limits of the electromagnetic end-cap calorimeters. The LAr forward calorimeters (FCal) extend the coverage to $|\eta| = 4.9$ with electromagnetic and hadronic energy measurements.

The muon spectrometer (MS) surrounds the calorimeters. It consists of three large superconducting air-core toroid magnets, precision tracking chambers providing accurate muon tracking out to $|\eta| = 2.7$, and fast detectors for triggering in the region $|\eta| < 2.4$.

A two-level trigger system is used to select events. A low-level hardware trigger reduces the data rate, and a high-level software trigger selects interesting final state events.

3 Data and Monte Carlo samples

3.1 Data

The dataset consists of proton-proton collisions at a centre-of-mass energy of 13 TeV, recorded by the ATLAS experiment at the LHC in 2015 and 2016. Requirements to ensure the quality of beam conditions, detector performance and data are imposed [7–9], as well as additional event cleaning criteria described in Section 8. After application of these criteria, the dataset corresponds to a total integrated luminosity of $36\,\mathrm{fb}^{-1}$.

3.2 Monte Carlo Samples

All samples of simulated events are passed through the ATLAS detector simulation [10] based on GEANT4 [10] and are reconstructed with the standard ATLAS reconstruction software. The effects of pileup from multiple interactions in the same and nearby bunch crossings are modelled by overlaying minimum-bias events, simulated using the soft QCD processes of PYTHIA 8.186 [11] with the A2 [12] set of tuned parameters (tune) and MSTW2008LO [13] parton distribution functions (PDF). For all samples of simulated events, except for those generated using SHERPA [14], the EvtGen v1.2.0 program [15] is used to describe the decays of bottom and charm hadrons. A summary of all the generators used for the simulation of the signal and background processes is shown in Table 1.

Simulation of Z bosons decaying to a pair of opposite sign leptons (e, μ, τ) is produced by SHERPA2.2.1 [14, 16, 17], and the simulation is normalised to the next-to-next to leading order cross-section [18]. The parton showering and hadronization are performed with SHERPA2.2.1 [19, 20]. The SHERPA Z boson simulation is considered as the default simulation throughout most of this note, except where mentioned otherwise. The POWHEG-BOX v2+PYTHIA8 [21] and MADGRAPH5_aMC@NLO 2.2.0+PYTHIA8 [22] Z boson simulation are used to compute the systematic uncertainties on the $E_{\mathrm{T}}^{\mathrm{miss}}$ soft term as discussed in Section 10. In addition to the full GEANT4 simulation of the ATLAS detector, dedicated systematic uncertainties are also derived for samples coming from fast calorimeter simulation (AFII) [23].

Table 1: Generators, cross-section normalizations, PDF sets, and MC tunes used in this analysis.

Sample	$Z \to \ell\ell$	$Z \to \ell\ell$	$Z \to \ell\ell$	$W \to \ell\nu$
Generator	SHERPA2.2.1 [14, 16, 17]	POWHEG-BOX v2+PYTHIA8 [21] + Photos++ 3.52 [24]	MADGRAPH5_aMC@NLO 2.2.0 [22]	SHERPA2.2.1
Use	Signal	Systematics	Systematics	Background
Cross-section order	NNLO [18]	NNLO	NNLO	NNLO
ME PDF set	NNPDF3.0NNLO [13]	CT10 [25]	NNPDF2.3LO [26]	NNPDF3.0NNLO
PS and Hadronization	SHERPA2.2.1 [19, 20]	PYTHIA 8.186 [11]	PYTHIA 8.186	SHERPA2.2.1
UE Model Tune	Default	AZNLO [27]	A14 [28]	Default

Sample	$t\bar{t}$	**s-channel top**	**t-channel top**	Wt**-channel top**
Generator	POWHEG-BOX v2	POWHEG-BOX v1 [29]	POWHEG-BOX v1	POWHEG-BOX v1 [30]
Use	Signal and background	Signal and background	Signal and background	Signal and background
Cross-section order	NNLO+NNLL [31, 32]	NLO [33]	NLO [34]	NLO [35]
ME PDF set	CT10	CT10f4	CT10f4	CT10f4
PS and Hadronization	PYTHIA 6.428 [36]	PYTHIA 6.428	PYTHIA 6.428	PYTHIA 6.428
UE Model Tune	P2012 [37]	P2012	P2012	P2012

Sample	$W^+W^- \to \ell^+\nu\ell^-\bar{\nu}$	$ZZ \to \ell\ell\nu\nu$	$WZ \to \ell\nu\ell\ell$	**VBF** $H \to WW^*$
Generator	POWHEG-BOX v2+PYTHIA8	POWHEG-BOX v2+PYTHIA8	POWHEG-BOX v2+PYTHIA8	POWHEG +PYTHIA8
Use	Background	Background	Background	Signal
Cross-section order	NNLO	NNLO	NNLO	NNLO
ME PDF set	CT10NLO	CT10NLO	CT10NLO	NNPDF30NNLO
PS and Hadronization	PYTHIA 8.186	PYTHIA 8.186	PYTHIA 8.186	CTEQ6L1 [38]
UE Model Tune	AZNLO	AZNLO	AZNLO	AZNLO

4 Event selection

The performance of $E_{\mathrm{T}}^{\mathrm{miss}}$ is studied in different event topologies. In particular, $E_{\mathrm{T}}^{\mathrm{miss}}$ signatures are generally distinguished between *true* E_T^{miss} *signatures*, in which the momentum imbalance is caused by prompt non-interacting particles escaping the detector, and *fake* E_T^{miss} *signatures*, caused by mismeasurement effects or similar.

4.1 $Z \to \ell\ell$ event selection

The $Z \to \ell\ell$ event topology is particularly convenient to study the fake $E_{\mathrm{T}}^{\mathrm{miss}}$ effects. The leptonic decay of the Z boson is not only extremely easy to trigger but also abundantly produced in pp collision and well modeled in the current ATLAS simulation. The $Z \to \ell\ell$ event selection criteria are:

- The lowest unprescaled ($p_{\mathrm{T}} > 24$ GeV in 2015 and $p_{\mathrm{T}} > 26$ GeV in 2016) single lepton (muon or electron) trigger is fired and at least one of the leptons matches to the trigger.
- The event contains exactly two opposite sign same flavor leptons consistent with the hard scatter interaction, passing "Medium" particle identification (PID) [39, 40], "Loose" isolation, and associated to the hard-scatter primary vertex (PV). The leading lepton in the pair is required to have $p_{\mathrm{T}} >$ 30 GeV and the sub-leading one $p_{\mathrm{T}} > 20$ GeV.
- No additional electrons or muons wth $p_{\mathrm{T}} > 7$ GeV and passing "Loose" PID are identified.
- The invariant mass of the di-lepton pair is consistent with the Z boson measured mass estimation within a window of 15 GeV: $|m_{\ell\ell} - m_Z| < 15$ GeV. Sections 6.6.1 and 10 use a window of 25 GeV to increase the sample size.
- Events with 1 or more jets after overlap removal with hard objects and failing the "BadLoose" criteria, which relates to jet cleaning as defined in Reference [9], are removed in data and simulation.
- Event cleaning from Section 8 is applied to data only.

4.2 $H \to WW$ event selection

The vector boson fusion (VBF) $H \to WW$ event topology is useful to study the performance of $E_{\mathrm{T}}^{\mathrm{miss}}$ in topologies with forward jets. Studies are performed in MC simulation only; thus the absence of background allows for very loose selection criteria. The following selection is applied:

- The lowest unprescaled ($p_{\mathrm{T}} > 24$ GeV in 2015 and $p_{\mathrm{T}} > 26$ GeV in 2016) single lepton (muon or electron) trigger is fired.
- The event contains exactly two opposite-sign same-flavor leptons, which are identified with "Medium" PID and "Loose" isolation selection criteria with $p_{\mathrm{T}} > 25$ GeV.
- No additional electrons or muons wth $p_{\mathrm{T}} > 7$ GeV and passing "Loose" PID are identified.

5 Definitions and reconstruction of $E_{\mathrm{T}}^{\mathrm{miss}}$

Different algorithms have been developed to reconstruct the $E_{\mathrm{T}}^{\mathrm{miss}}$ in ATLAS. They differ in the information used to reconstruct the p_{T} of the particles, using either energy deposits in the calorimeters, tracks reconstructed in the ID or different combinations of both.

The $E_{\mathrm{T}}^{\mathrm{miss}}$ reconstruction estimates the amount of missing transverse momentum in the detector using calibrated detector signals corresponding to muons (μ), electrons (e), photons (γ), hadronically decaying τ-leptons, and jets. The missing transverse momentum vector $\vec{E}_{\mathrm{T}}^{\mathrm{miss}}$ is calculated using the components along the x and y axes:

$$E_{x(y)}^{\mathrm{miss}} = E_{x(y)}^{\mathrm{miss},\mu} + E_{x(y)}^{\mathrm{miss},e} + E_{x(y)}^{\mathrm{miss},\gamma} + E_{x(y)}^{\mathrm{miss},\tau} + E_{x(y)}^{\mathrm{miss,jets}} + E_{x(y)}^{\mathrm{miss,soft}}, \tag{1}$$

where each term is calculated as the negative vectorial sum of transverse momenta of energy deposits or trajectories of charged particles. Energy deposits in the calorimeters and tracks are matched to reconstructed objects in an order chosen to minimise double-counting of detector signals. The most commonly used order for the $E_{\mathrm{T}}^{\mathrm{miss}}$ reconstruction sequence for the hard-object contribution starts with muons, electrons, followed by photons, then hadronically decaying τ-leptons, and finally jets. Muons are principally reconstructed from ID and MS tracks alone, with corrections based on their energy loss in the calorimeter, leading to little or no signal overlap with the other reconstructed particles in the calorimeter. Details on the treatment of these small overlapping signals are presented in Section 6.6.2. The signals not associated with reconstructed objects form the *soft term*, whereas those associated with the reconstructed objects are collectively referred to as the *hard term*.

The vector $\vec{E}_{\mathrm{T}}^{\mathrm{miss}}$ provides the amount of the missing transverse momentum via its magnitude $E_{\mathrm{T}}^{\mathrm{miss}}$ and its direction in the transverse plane in terms of the azimuthal angle ϕ^{miss}.

The total transverse energy in the detector $\sum E_{\mathrm{T}}$ quantifies the total event activity. It is an important observable for understanding the resolution of the $E_{\mathrm{T}}^{\mathrm{miss}}$, especially with increasing pileup contributions, and is defined as the scalar sum of the transverse momenta of reconstructed objects and soft-term signals that contribute to the $E_{\mathrm{T}}^{\mathrm{miss}}$ reconstruction:

$$\sum E_{\mathrm{T}} = \sum p_{\mathrm{T}}^{\mu} + \sum p_{\mathrm{T}}^{e} + \sum p_{\mathrm{T}}^{\gamma} + \sum p_{\mathrm{T}}^{\tau} + \sum p_{\mathrm{T}}^{\mathrm{jets}} + \sum p_{\mathrm{T}}^{\mathrm{soft}}, \tag{2}$$

5.1 Definition of $E_{\mathrm{T}}^{\mathrm{miss}}$ resolution

The $E_{\mathrm{x}}^{\mathrm{miss}}$ and $E_{\mathrm{y}}^{\mathrm{miss}}$ are expected to be approximately Gaussian distributed for $Z \to \ell\ell$ events as discussed in Reference [2], with deviations arising from noise and events with large $\sum E_{\mathrm{T}}$. However, because these distributions have non-Gaussian tails, the root-mean-square (RMS) is used to estimate the resolution. The RMS includes important information about the $E_{\mathrm{T}}^{\mathrm{miss}}$ tails which would be lost if the result of a Gaussian fit over only the core of the distribution is used. The resolution of the $E_{\mathrm{T}}^{\mathrm{miss}}$ distribution is extracted using the RMS from the combined distribution of $E_{\mathrm{x}}^{\mathrm{miss}}$ and $E_{\mathrm{y}}^{\mathrm{miss}}$. For processes with real $E_{\mathrm{T}}^{\mathrm{miss}}$, the true $E_{\mathrm{x}}^{\mathrm{miss}}$ and $E_{\mathrm{y}}^{\mathrm{miss}}$ are subtracted from their reconstructed quantities in simulation.

6 The $E_{\mathrm{T}}^{\mathrm{miss}}$ hard term

Each reconstructed hard object has its own dedicated calibration, translating the detector signals into a fully corrected four-momentum. A subset of these reconstructed particles are then selected for physics analysis using quality or isolation criteria in order to reject fake or otherwise problematic signatures. The hard term of the $E_{\mathrm{T}}^{\mathrm{miss}}$ is computed from the selected muons, electrons, photons, hadronically decaying τ-leptons[4], and jets in each event.

The specific particle and jet selections in a given analysis must be reflected in the $E_{\mathrm{T}}^{\mathrm{miss}}$ for a consistent interpretation of a given event. For example, the electron selection applied in a given analysis must be applied consistently also to the $E_{\mathrm{T}}^{\mathrm{miss}}$ reconstruction. The selection of reconstructed non-jet objects are interpreted (and therefore calibrated) as electrons rather than as hadronic jets in the $E_{\mathrm{T}}^{\mathrm{miss}}$ reconstruction. The selection criteria used in this note and defined below are typical but not universal. The performance measurements for the $E_{\mathrm{T}}^{\mathrm{miss}}$ as defined and presented in this note are therefore representative of most ATLAS searches and measurements.

The prescriptions for using reconstructed photons and hadronically decaying τ-leptons are discussed. However, no reconstructed photons nor hadronically decaying τ-leptons are used in the definition of the $E_{\mathrm{T}}^{\mathrm{miss}}$ in this note, which means that their corresponding detector signals are treated as if arising from hadronic jets. The topologies considered do not have a large production of either object, so their contributions were found to be negligible in the core as well as the tails of the distributions in this note. However, in analyses specifically requiring these objects they will typically use them in their $E_{\mathrm{T}}^{\mathrm{miss}}$ definition. Some $E_{\mathrm{T}}^{\mathrm{miss}}$ distributions built using these objects can be found in References [41] and [42].

6.1 Muons

Muon candidates are identified by matching an ID track with an MS track or segment [40]. Muons are required to satisfy $p_{\mathrm{T}} > 10$ GeV to be included in the $E_{\mathrm{T}}^{\mathrm{miss}}$ reconstruction. Since muon track p_{T} is corrected for energy losses in the detector as described in Section 6.6.2, any muon energy deposited in the calorimeter is taken into account using either parameterised estimates or direct measurements to prevent double-counting [4, 40].

6.2 Electrons

Electrons are reconstructed from clusters in the electromagnetic (EM) calorimeter which are associated with an ID track [39]. Electron identification is restricted to the range of $|\eta| < 2.47$, excluding the transition region between the barrel and end-cap EM calorimeters, $1.37 < |\eta| < 1.52$. They are calibrated at the EM scale[5] [43] as well as additional simulation-based and in-situ corrections [44]. Electrons satisfying the "Medium" likelihood [39] and "Loose" isolation selection criteria with $p_{\mathrm{T}} > 10$ GeV are included in the $E_{\mathrm{T}}^{\mathrm{miss}}$ reconstruction for the studies presented in this note.

[4] This term consists of reconstructed 3-prong and 1-prong hadronically decaying τ-leptons.

[5] The EM scale is the nominal signal scale for the ATLAS calorimeters. It accounts correctly for the energy deposited by EM showers in the calorimeter, but it does not consider energy losses in the un-instrumented material or invisible energy deposits in hadronic showers.

6.3 EMTopo jets

Jets are reconstructed from three-dimensional topological clusters (topoclusters) [45] of energy deposits in the calorimeter using the anti-k_t algorithm [46] with a distance parameter $R = 0.4$. The topoclusters are calibrated at the EM energy scale. The jets are fully calibrated using the EM+JES scheme [47] including a correction for pileup [48]. These EMTopo jets are required to have $p_{\mathrm{T}} > 20$ GeV after the full calibration. The matching of tracks with jets is performed via ghost association, where tracks are clustered as ghost particles into the jet, as described in Reference [3] and based on the approach outlined in Reference [49].

Jets are further filtered using a tagging algorithm to select hard-scatter jets [48]. The jet vertex tagging (JVT) algorithm provides a likelihood discriminant[6] using observables derived from the tracks matched to each jet. In the calculation of the JVT discriminant the total amount of p_{T} carried by tracks from the hard-scatter vertex and matched to the given jet is related to the total amount of p_{T} carried by all matched tracks, among other inputs, to tag jets from the hard-scatter interaction. After proper jet calibration and reconstruction, this quantity is used to reject pileup for jets by requiring JVT > 0.59 for jets with $p_{\mathrm{T}} < 60$ GeV and $|\eta| < 2.4$.

The forward-jet-vertex tagger (fJVT) [50] is an approach to remove jets with $|\eta| > 2.5$ and $20 < p_{\mathrm{T}} < 50$ GeV coming from pileup interactions. The fJVT uses the angular kinematics of other jets in the event to associate forward jets, which do not have tracking information, to pileup vertices by minimizing the other vertex's reconstructed $E_{\mathrm{T}}^{\mathrm{miss}}$. In this note, the fJVT selection criteria is not used unless specified, as in Section 9.

6.4 PFlow jets

Particle Flow (or PFlow) reconstruction of objects is particularly useful for the $E_{\mathrm{T}}^{\mathrm{miss}}$ measurement as it reflects the use of the highest quality signals from the calorimeter and the ID. This approach combines the measurements from the inner detector and calorimeter to reconstruct the energy flow of the event to improve jet measurements as opposed to simply using track based corrections in the jet calibration.

The PFlow algorithm suppresses calorimeter energy deposits arising from charged pileup particles and takes the momentum estimation from tracks whenever the tracker resolution is better than the calorimeter resolution. PFlow jets are constructed with the anti-k_t algorithm with a $R = 0.4$ radius using charged constituents associated with the primary vertex and neutral PFlow constituents as inputs. This strategy offers significant improvements of the jet energy resolution, reduced pileup jet rates, and a more accurate jet direction in the (η, ϕ) plane. The PFlow algorithm is described in detail in Reference [5]. After proper jet calibration and reconstruction, the PFlow jets are associated to the hard-scatter interaction with the JVT required to be larger than 0.2 for jets with $p_{\mathrm{T}} < 60$ GeV and $|\eta| < 2.4$. This selection criteria has the same pileup jet rejection as the tighter JVT selection for EMTopo jets with a higher hard-scatter jet efficiency.

The $E_{\mathrm{T}}^{\mathrm{miss}}$ may be built with either EMTopo jets or PFlow jets. As tracks associated to electrons or muons are not considered in the PFlow shower subtraction, no differences are expected for the $E_{x(y)}^{\mathrm{miss},\mu}$ and $E_{x(y)}^{\mathrm{miss},e}$ components with respect to the EMTopo $E_{\mathrm{T}}^{\mathrm{miss}}$. On the other hand, the jet and the soft term can significantly benefit from the utilisation of PFlow constituents as defined in Section 7.2. These terms represent the major changes of PFlow $E_{\mathrm{T}}^{\mathrm{miss}}$ with respect to the EMTopo $E_{\mathrm{T}}^{\mathrm{miss}}$.

[6] The JVT score ranges from 0 (pileup-like) to 1 (hard-scatter-like).

6.5 Definition of the $E_{\mathrm{T}}^{\mathrm{miss}}$ operating point

The *Loose* $E_{\mathrm{T}}^{\mathrm{miss}}$ working point, which is used throughout this note unless otherwise indicated, uses the same jet selection as in Reference [4], and includes all jets with $p_{\mathrm{T}} > 20$ GeV that also pass the JVT criteria when the jet has $|\eta| < 2.4$ and $p_{\mathrm{T}} < 60$ GeV. This applies to $E_{\mathrm{T}}^{\mathrm{miss}}$ built with both EMTopo and PFlow jets.

6.6 Overlap removal

In the calculation of $E_{\mathrm{T}}^{\mathrm{miss}}$ and $\sum E_{\mathrm{T}}$ the contributing objects need to be reconstructed from mutually exclusive detector signals to avoid multiple inclusions of the same signal in constructed observables. Energy deposits in the detector systems need to be correctly assigned to the particles or jets that generated them. When hard objects are produced close-by in the detector, shared or overlapping energy deposits must be resolved, and their treatment is specified in Sections 6.6.1 and 6.6.2.

Topoclusters from jets are matched to other objects using a ΔR matching. For hadronically-decaying τ-leptons, topoclusters within a $\Delta R < 0.2$ of the jet used to seed the hadronic τ reconstruction are matched. For electrons and photons, the matching is more complex and uses an iterative procedure. For topoclusters with $\Delta R < 0.1$ of the electron or photon candidate the subset of topoclusters that match best to the candidate's energy is chosen. The best-matching procedure proceeds as follows starting from the highest p_{T} topocluster and iterating to the lowest p_{T} one:

- Topoclusters are associated to a candidate if they have energy less than 1.5 times the candidate's energy and if adding the topocluster energy to a running sum reduces the difference between the sum of topocluster energy and the candidate's energy.
- If no topoclusters have energy less than 1.5 times the candidate's energy, then only the topocluster with energy closest to the candidate's energy is associated to the candidate.

6.6.1 Jet and e/γ signal ambiguity resolution

All electrons passing the selection described in Section 6.2 enter the $E_{\mathrm{T}}^{\mathrm{miss}}$ reconstruction as the highest priority signature in the calorimeter. The lower-priority reconstructed particles (γ, τ-leptons, and jets added in order of priority) are fully rejected if they share their calorimeter signal (e.g. topoclusters are ΔR matched to the hard objects as described above) with a higher-priority object that has already entered the $E_{\mathrm{T}}^{\mathrm{miss}}$ reconstruction. Generally, jets are rejected if they overlap with accepted higher-priority particles. As such, the jet contribution to $E_{\mathrm{T}}^{\mathrm{miss}}$ is dependent on the signal ambiguity resolution. Fake missing transverse momentum can arise in cases where electrons, photons or hadronically-decaying τ-leptons are close to jets. In previously used $E_{\mathrm{T}}^{\mathrm{miss}}$ definitions [4], the quantity that decided the amount of a jet's energy signature that was treated as a real jet and assigned to the $E_{\mathrm{T}}^{\mathrm{miss}}$ jet term was the ratio f_{overlap} of the electron (photon or hadronically decaying τ-leptons) energy $E_{e(\gamma,\tau)}^{\mathrm{EM}}$ to the jet energy $E_{\mathrm{jet}}^{\mathrm{EM}}$:

$$f_{\mathrm{overlap}} = \frac{E_{e(\gamma,\tau)}^{\mathrm{EM}}}{E_{\mathrm{jet}}^{\mathrm{EM}}} \tag{3}$$

with both energies calibrated at the EM scale. The variable f_{overlap} represents the electron (photon, hadronically decaying τ-lepton) energy fraction in a given jet, and it is used to determine the amount of

the jet energy signatures that should be used in the $E_{\mathrm{T}}^{\mathrm{miss}}$ reconstruction. The case of $f_{\mathrm{overlap}} \leq 0.5$ may arise from a higher p_{T} jet near an electron, and the jet is included in $E_{\mathrm{T}}^{\mathrm{miss}}$ reconstruction with its p_{T} scaled by f_{overlap}. For $f_{\mathrm{overlap}} > 0.5$ the jet was assigned to the soft term, and only the tracks associated with the jet were included in the $E_{\mathrm{T}}^{\mathrm{miss}}$ calculation.

This procedure is problematic if both the jet and electron, photon or hadronically decaying τ-lepton are real and overlapping, as the soft term in this note is track-based only and does not account for neutral particles. Neutral energy is lost and manifests as spurious $E_{\mathrm{T}}^{\mathrm{miss}}$. Here the overlap between electrons and jets is discussed primarily, but the procedure is applied similarly to γ and hadronically decaying τ-leptons. For electrons and jets with $\Delta R(e, \mathrm{jet}) < 0.4$, the $E_{\mathrm{T}}^{\mathrm{miss}}$ tails above 200 GeV are dominated by jets with $f_{\mathrm{overlap}} > 0.5$ because around half of the jet p_{T} was not being included in the $E_{\mathrm{T}}^{\mathrm{miss}}$ reconstruction.

The $E_{\mathrm{T}}^{\mathrm{miss}}$ calculation may be improved by reducing the number of real jets that are wrongly assigned to the soft term. This was studied in simulation. An additional discriminating variable $\Delta p_{\mathrm{T}}^{\mathrm{EM},e(\gamma,\tau),\mathrm{jet}}$, defined in Equation 4, is used, represents the unique p_{T} of the jet and is calculated as the p_{T} difference at the EM scale of the jet and electron:

$$\Delta p_{\mathrm{T}}^{\mathrm{EM},e(\gamma,\tau),\mathrm{jet}} = p_{\mathrm{T}}^{\mathrm{EM,jet}} - p_{\mathrm{T}}^{\mathrm{EM},e(\gamma,\tau)}. \tag{4}$$

A scan is performed for selection criteria on f_{overlap} and $\Delta p_{\mathrm{T}}^{\mathrm{EM},e(\gamma,\tau),\mathrm{jet}}$. The optimisation is performed on data and simulation applying the Z event selection from Section 4.1.

Using $f_{\mathrm{overlap}} < 1.0$, and $\Delta p_{\mathrm{T}}^{\mathrm{EM},e(\gamma,\tau),\mathrm{jet}} > 20$ GeV as condition for the jet to be treated as a real jet and put into the jet term, the tails are significantly reduced, as shown in Figure 1. The reduction of the $E_{\mathrm{T}}^{\mathrm{miss}}$ tails above 200 GeV is found to be about 30% in $Z \rightarrow ee$ simulated events.

6.6.2 Jet and μ signal ambiguity resolution

Muons experience energy loss in the calorimeters, but only non-isolated muons overlap with other hard objects, typically jets or hadronically decaying τ-leptons. Tagging jets using JVT efficiently retains those from the hard-scatter primary vertex for $E_{\mathrm{T}}^{\mathrm{miss}}$ reconstruction and rejects jets generated by pileup. However, a muon overlapping with a pileup jet can lead to a mis-tag, because the ID track from the muon represents a significant amount of p_{T} from the hard-scatter vertex and thus increases the JVT value. In this case the pileup jet p_{T} contributes to $E_{\mathrm{T}}^{\mathrm{miss}}$, degrading both the $E_{\mathrm{T}}^{\mathrm{miss}}$ response and resolution due to the stochastic nature of its contribution.

Muons can also occasionally experience a significant energy loss in the calorimeter which is reconstructed as a hard-scatter jet from the primary vertex. This jet is found in close proximity to the ID track associated with the muon. Inclusion of such a jet into $E_{\mathrm{T}}^{\mathrm{miss}}$ reconstruction leads to double-counting of the transverse momentum associated with the muon energy loss, as the fully reconstructed muon p_{T} is already corrected for this effect.

To reject contributions from pileup jets and jets reconstructed from muon energy loss, the following selection criteria are applied:

- the ID track of the muon is "ghost"-associated to the jet using the anti-k_t algorithm [46] ;
- $p_{\mathrm{T}}^{\mu-\mathrm{ID}}/p_{\mathrm{T}}^{\mathrm{jet}-\mathrm{ID}} > 0.8$ – the transverse momentum of the ID track associated with the muon ($p_{\mathrm{T}}^{\mu-\mathrm{ID}}$) represents a significant fraction of the transverse momentum $p_{\mathrm{T}}^{\mathrm{jet}-\mathrm{ID}}$, the sum of the transverse momenta of all ID tracks emerging from the hard-scatter PV associated with the jet;

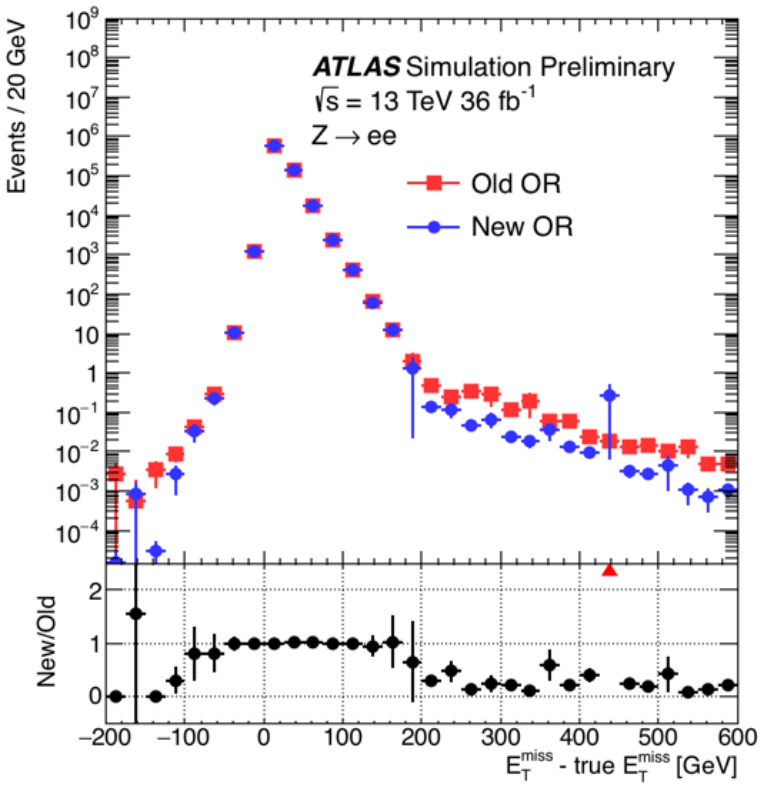

Figure 1: Comparison of $E_{\mathrm{T}}^{\mathrm{miss}}$ performance between old (red) and new (blue) jet and electron/photon/hadronically decaying τ-lepton overlap removal (OR) procedure in $\mathrm{Z} \rightarrow ee$ simulation. The $E_{\mathrm{T}}^{\mathrm{miss}}$ tails are diminished with the new technique, indicating that fake $E_{\mathrm{T}}^{\mathrm{miss}}$ has been reduced.

- $p_{\mathrm{T}}^{\mathrm{jet}}/p_{\mathrm{T}}^{\mu-\mathrm{ID}} < 2$ – the overall transverse momentum $p_{\mathrm{T}}^{\mathrm{jet}}$ of the jet is not too large compared to $p_{\mathrm{T}}^{\mu-\mathrm{ID}}$;
- $N_{\mathrm{track}}^{\mathrm{PV}} < 5$ – the total number of tracks $N_{\mathrm{track}}^{\mathrm{PV}}$ associated with the jet and emerging from the hard-scatter PV is small.

All jets with overlapping muons meeting all of these criteria are considered to be either from pileup or a catastrophic muon energy loss and are rejected for $E_{\mathrm{T}}^{\mathrm{miss}}$ reconstruction. The corresponding muons enter into the $E_{\mathrm{T}}^{\mathrm{miss}}$ calculation.

Another consideration for muon contributions to $E_{\mathrm{T}}^{\mathrm{miss}}$ is Final-State Radiation (FSR). Muons can radiate hard photons at small angles, which are typically not reconstructed as photons because of the nearby muon ID track violating photon isolation requirements. They are also not reconstructed as electrons, due to the mismatch between the ID track momentum and the energy measured by the calorimeter. The calorimeter signal generated by the FSR photon is reconstructed as a jet with an associated muon ID track. As the transverse momentum carried by the FSR photon is not recovered in muon reconstruction, jets representing this photon need to be included in the $E_{\mathrm{T}}^{\mathrm{miss}}$ reconstruction. Such jets are characterised by the following selections, which are highly indicative of a photon in the ATLAS calorimeters:

- the ID track of the muon is "ghost"-associated to the jet using the anti-k_t algorithm [46] ;

- $N_{\text{track}}^{\text{PV}} < 3$ – the jet has low charged-particle content, indicated by a very small number of tracks from the hard-scatter PV;
- $f_{\text{EM}} > 0.9$ – the jet energy E_{jet} is largely deposited in the electromagnetic (EM) calorimeter, as expected for photons and measured by the corresponding energy fraction $f_{\text{EM}} = E_{\text{jet}}^{\text{EM}}/E_{\text{jet}}$;
- $p_{\text{T}}^{\text{jet PS}} > 2.5$ GeV – the large transverse momentum contribution of the jet in the presampler (PS) calorimeter ($p_{\text{T}}^{\text{jet PS}}$) layer indicates an early starting point for the shower;
- $w_{\text{jet}} < 0.1$ – the jet is narrow, with a width w_{jet} comparable to a dense electromagnetic shower; w_{jet} is defined as:

$$w_{\text{jet}} = \frac{\sum_i \Delta R_i p_{\text{T},i}}{\sum_i p_{\text{T},i}}, \tag{5}$$

  where $\Delta R_i = \sqrt{(\Delta\eta_i)^2 + (\Delta\phi_i)^2}$ is the angular distance of topocluster i from the jet axis, and $p_{\text{T},i}$ is the transverse momentum of this cluster;
- $p_{\text{T}}^{\text{jet–ID}}/p_{\text{T}}^{\mu\text{–ID}} > 0.8$ – the transverse momentum $p_{\text{T}}^{\text{jet–ID}}$ carried by all tracks emerging from the hard-scatter PV and associated with the jet is close to $p_{\text{T}}^{\mu\text{–ID}}$.

Jets are accepted for $E_{\text{T}}^{\text{miss}}$ reconstruction when found to be consistent with an FSR photon as defined by meeting all of the above selection criteria. Their energy scale is set to the EM scale to correctly reflect the interpretation as a photon.

7 The $E_{\text{T}}^{\text{miss}}$ soft term

The soft term is a necessary but challenging ingredient of the $E_{\text{T}}^{\text{miss}}$ reconstruction. It is comprised of all detector signals not matched to the reconstructed objects defined previously and may contain contributions from the hard scatter as well as the underlying event and pileup interactions.

7.1 The track-based soft term for EMTopo $E_{\text{T}}^{\text{miss}}$

Several algorithms used in the past have been designed to reconstruct the soft term [2, 3], but all $E_{\text{T}}^{\text{miss}}$ definitions described in this note use a track-based soft term (TST). The TST includes contributions from tracks not associated to hard objects.

Tracks are associated to the hard scatter vertex by considering the longitudinal and the transverse impact parameters d_0 and z_0 defined with respect to the hard scatter vertex position. d_0 is defined as the shortest distance in the transverse plane from a track to the beam line, and z_0 is the z-coordinate of the track point closest to the beam line. The selections are summarised in Table 2.

$p_{\text{T}} > 0.4$ GeV
$\lvert\eta\rvert < 2.5$ (ATLAS detector coverage for the ID tracking volume)
$\left\lvert\frac{d_0}{\sigma(d_0)}\right\rvert < 2$
$\lvert z_0 \sin(\theta)\rvert < 3.0$ mm

Table 2: Track selections for the TST.

These criteria provide excellent track-to-vertex matching for the soft term. By not including the neutral contributions, the track-based reconstruction entirely removes the out-of-time pileup contributions that affect neutral soft term algorithms [2, 3].

To avoid double counting particles, the tracks matched to the high-p_{T} reconstructed objects defined in Section 6 need to be removed from the soft term. All of the following classes of tracks are excluded from the soft term[7]:

- tracks within $\Delta\eta < 0.2$ and $\Delta\phi < 0.05$ around electrons and photons[8];
- tracks within a cone of size $\Delta R = 0.2$ around hadronically decaying τ-leptons;
- ID tracks associated with identified muons;
- tracks matched to jets using the ghost association technique described in Section 6;
- isolated tracks with $p_{\mathrm{T}} > 120$ GeV (> 200 GeV for $|\eta| < 1.5$) having estimated relative resolution on their p_{T} larger than 40% or having no associated calorimeter energy deposit with p_{T} larger than 65% of the track p_{T}[9]. This is a cleaning cut to remove mismeasured tracks.

7.2 The track-based soft term for PFlow $E_{\mathrm{T}}^{\mathrm{miss}}$

The $E_{\mathrm{T}}^{\mathrm{miss}}$ built using PFlow jets instead of EMTopo jets uses a slightly different definition of the TST. Analogous to the standard track-based soft term reconstruction, the PFlow-based soft term (PFlow TST) uses tracks associated to charged PFlow constituents which are not associated to any well-identified reconstructed object and surviving the track-to-vertex association. Tracks entering in PFlow TST have similar requirements to the ones used in the EMTopo-based approach including the same track-to-hard-object association as described in Section 7. Any differences are due to the different tracks quality requirements considered by the PFlow algorithm and also to the different track-to-vertex association. However, a comparison between the EMTopo-based and the PFlow-based TST showed minimal differences between these two terms. The different track quality requirements are summarised as follows:

- $p_{\mathrm{T}} > 0.5$ GeV,
- $|\eta| < 2.5$,
- $|z_0 \sin(\theta)| < 2.0$ mm.

No requirement on the transverse track parameter d_0 is applied for PFlow TST or in the PFlow algorithm to avoid biases on displaced jets. The increased track p_{T} threshold from 0.4 GeV in Section 7.1 to 0.5 GeV for the PFlow TST does not have a significant impact on the performance of the soft term reconstruction.

[7] The photon and hadronically decaying τ-leptons are shown for illustration but are not used in this note.
[8] The precise selections are more stringent than radial distance selections, and the details are given in Reference [51].
[9] The p_{T} thresholds are chosen to ensure that muons failing quality requirements or not in the coverage of the MS, for example in the gaps between detectors, are still included in the soft term.

8 Electronics saturation in electromagnetic end-cap calorimeter

In high pileup data collected in 2016, the bunch train structure, which included 8 filled followed by four empty bunches, introduced saturation in the electronics of the inner wheel of the electromagnetic calorimeter end-cap (EMEC-IW), which lies in the region $2.5 < |\eta| < 3.2$. This phenomenon occurred at the end of the bunch train with the electronics remaining in a saturated state for the start of the next bunch train. The electronics then recovered over the first few bunch crossings.

This results in two effects. First, the calorimeter energy is observed to be lower for the first two crossings. Second, as the EMEC-IW readout electronics recover, large electronic noise is observed in next few crossings. The first effect is small for jets and corrected for in electron energy calibration. However, the second effect results in many fake jets being reconstructed in the corresponding η region in a small fraction of data from the beginning of bunch trains, and spurious jets result in fake $E_{\mathrm{T}}^{\mathrm{miss}}$. This effect is not present in the simulation. Figures 2(a) and 2(b) show the η of the sub-leading jet in events more than four jets in data and simulation and the jet multiplicity in data and simulation. Greater numbers of jets are observed in data for this region of the detector.

A cleaning criterion is defined to remove these events in both EMTopo and PFlow jets and to reduce the corresponding spurious $E_{\mathrm{T}}^{\mathrm{miss}}$ tail. Problematic clusters are identified by requiring $p_{\mathrm{T}}^{\mathrm{EM}} > 0.5$ GeV and $\langle Q_{\mathrm{LAr}} \rangle > 0.2$, where $\langle Q_{\mathrm{LAr}} \rangle$ is the energy-squared weighted average of the cells liquid argon quality [9]. Events which contain more than 20 of these clusters within $2.5 < |\eta| < 3.2$ are vetoed to remove events suffering from EMEC-IW saturation. The cleaning criterion is applied to data only and not to simulation.

The efficiency of this cleaning criterion is measured to be 98.34% in $Z \rightarrow \mu\mu$, a topology which exhibits no significant bias to calorimeter problems. This cleaning criterion effectively reduces the luminosity by $(1.7 \pm 1.1)\%$ where the uncertainty arises from the dependence of the efficiency on the physics process.

The effectiveness of the EMEC-IW cleaning can be seen in Figure 2(c) where the η spectrum of the sub-leading jet in events with more than four jets is shown with the cleaning applied. The ratio of data to simulation differences in the relevant η region are reduced. The increasing trend in the ratio of data to simulation for jet multiplicities larger than seven, as shown in Figure 2(b), is removed after applying the cleaning as seen in Figure 2(d). The $E_{\mathrm{T}}^{\mathrm{miss}}$ is affected by these spurious jets, and Figure 2(e) shows the $E_{\mathrm{T}}^{\mathrm{miss}}$ distribution with the "Loose" $E_{\mathrm{T}}^{\mathrm{miss}}$ definition, as defined in Section 6.5, for events with more than four jets with and without this additional cleaning. The events with $E_{\mathrm{T}}^{\mathrm{miss}}$ of about 100 GeV are reduced by about 40% while events with higher $E_{\mathrm{T}}^{\mathrm{miss}}$ of more than 200 GeV, which mostly come from real $E_{\mathrm{T}}^{\mathrm{miss}}$ processes, are largely unaffected.

9 Working points for $E_{\mathrm{T}}^{\mathrm{miss}}$

The selection of jets used to calculate the $E_{\mathrm{T}}^{\mathrm{miss}}$ has a large impact on $E_{\mathrm{T}}^{\mathrm{miss}}$ performance. To offer different working points for physics analyses with different requirements, a few alternative $E_{\mathrm{T}}^{\mathrm{miss}}$ definitions are studied.

As defined in Section 6.5, the *Loose* $E_{\mathrm{T}}^{\mathrm{miss}}$ working point includes all jets with $p_{\mathrm{T}} > 20$ GeV that also pass the JVT criteria when the jet has $|\eta| < 2.4$ and $p_{\mathrm{T}} < 60$ GeV.

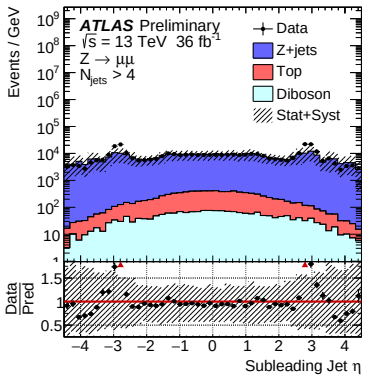

(a) The η of the sub-leading jet in events with greater than four jets in a $Z \rightarrow \mu\mu$ selection without any cuts to remove saturation problems in the EMEC-IW.

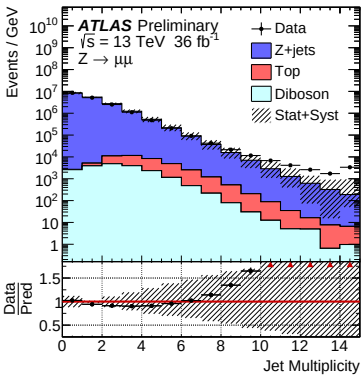

(b) The jet multiplicity in a $Z \rightarrow \mu\mu$ event selection without any cuts to remove saturation problems in the EMEC-IW.

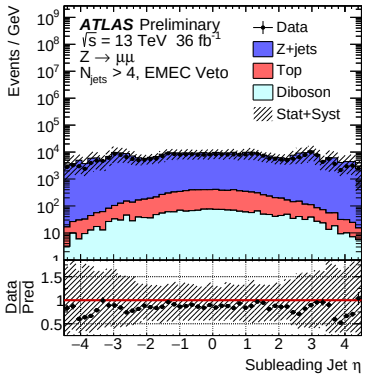

(c) The η of the sub-leading jet in events with greater than four jets in a $Z \rightarrow \mu\mu$ selection with the cuts to remove saturation problems in the EMEC-IW applied.

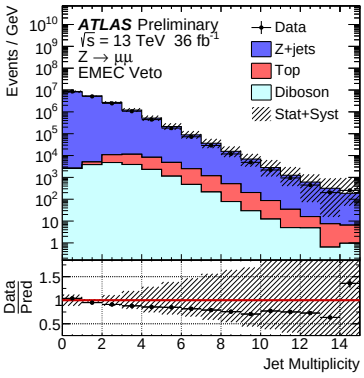

(d) The jet multiplicity in a $Z \rightarrow \mu\mu$ event selection with cuts to remove saturation problems in the EMEC-IW applied.

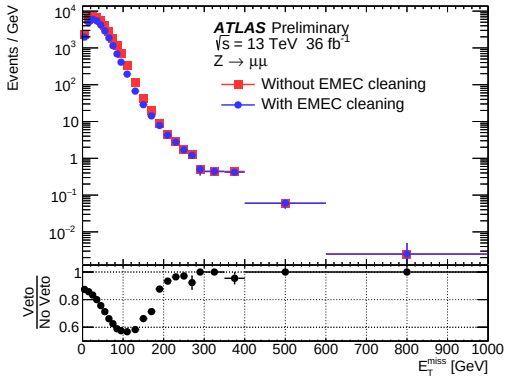

(e) A comparison of the $E_{\mathrm{T}}^{\mathrm{miss}}$ in data for events with greater than four jets in a $Z \rightarrow \mu\mu$ selection with and without the cuts to remove saturation problems in the EMEC-IW applied.

Figure 2: The impact of the cuts designed to remove affected by the saturation problems in the EMEC-IW.

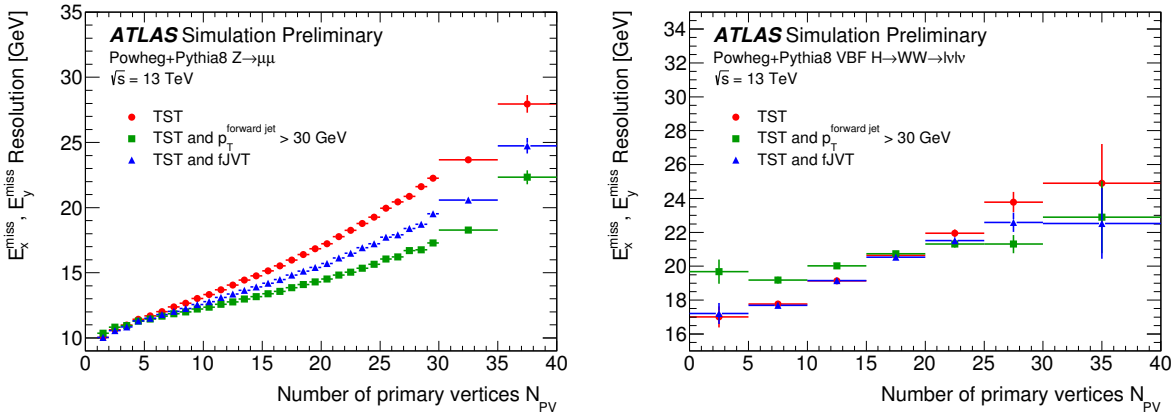

(a) (b)

Figure 3: Distributions of the $E_{\mathrm{T}}^{\mathrm{miss}}$ resolution versus N_{PV} for $E_{\mathrm{T}}^{\mathrm{miss}}$ built with three different forward jet selections in a $Z \rightarrow \mu\mu$ (left) and VBF $H \rightarrow WW$ (right) simulation. TST $E_{\mathrm{T}}^{\mathrm{miss}}$ denotes the $E_{\mathrm{T}}^{\mathrm{miss}}$ built with the standard selection for jets as previously defined. The $E_{\mathrm{T}}^{\mathrm{miss}}$ resolution is defined in Section 5.1.

A second *Tight* working point was developed to reduce the pileup dependence of $E_{\mathrm{T}}^{\mathrm{miss}}$. Tight $E_{\mathrm{T}}^{\mathrm{miss}}$ is calculated without including forward jets with $|\eta| > 2.4$ and $20 < p_{\mathrm{T}} < 30$ GeV. This tighter threshold removes regions of phase space that have more pileup jets than hard scatter jets. However, because hard-scatter jets may also be removed, the scale of the reconstructed $E_{\mathrm{T}}^{\mathrm{miss}}$ would be degraded. Additionally, the resolution is worse at low pileup when a larger fraction of the removed jets are hard-scatter jets. Nevertheless this method can offer improved $E_{\mathrm{T}}^{\mathrm{miss}}$ resolution in high pileup conditions.

In Section 6.3 the fJVT algorithm is described, and it suppresses forward pileup jet contamination. A third Forward-JVT (fJVT) [52] $E_{\mathrm{T}}^{\mathrm{miss}}$ working point is also available to suppress tails in the $E_{\mathrm{T}}^{\mathrm{miss}}$. The fJVT $E_{\mathrm{T}}^{\mathrm{miss}}$ keeps the jet p_{T} requirement of greater than 20 GeV but is calculated without including forward jets with $|\eta| > 2.5$, $20 < p_{\mathrm{T}} < 50$ GeV and failing the "Loose" fJVT criteria, as defined in Reference [52]. The JVT requirement is applied to jets with $|\eta| < 2.4$ and $p_{\mathrm{T}} < 60$ GeV.

These modifications to the EMTopo $E_{\mathrm{T}}^{\mathrm{miss}}$ are studied in two topologies, shown in Figure 3. The $E_{\mathrm{T}}^{\mathrm{miss}}$ resolution, defined in Section 5.1, is studied in events with zero true $E_{\mathrm{T}}^{\mathrm{miss}}$ in $Z \rightarrow \mu\mu$ simulation in Figure 3(a) and in events with forward hard scatter jets with a vector boson fusion (VBF) $H \rightarrow WW$ simulation in Figure 3(b), following the event selections described in Sections 4.1 and 4.2, respectively. In both event topologies, raising the forward jet p_{T} cut to 30 GeV reduces the slope of the $E_{\mathrm{T}}^{\mathrm{miss}}$ resolution versus N_{PV}. The loose operating point of the fJVT also improves the $E_{\mathrm{T}}^{\mathrm{miss}}$ resolution. In the VBF $H \rightarrow WW$ simulation at low N_{PV}, increasing the forward jet p_{T} cut to 30 GeV removes hard-scatter jets from the VBF physics process and degrades the $E_{\mathrm{T}}^{\mathrm{miss}}$ resolution.

10 Systematic uncertainties

As $E_{\mathrm{T}}^{\mathrm{miss}}$ is a topological event quantity, the $E_{\mathrm{T}}^{\mathrm{miss}}$ uncertainty is computed using the systematics associated to each object entering the $E_{\mathrm{T}}^{\mathrm{miss}}$ reconstruction. For the hard component, systematic uncertainties on each reconstructed object are propagated to the $E_{\mathrm{T}}^{\mathrm{miss}}$ as part of $E_{\mathrm{T}}^{\mathrm{miss}}$ reconstruction. However, the soft

term estimation is fully specified by the $E_{\mathrm{T}}^{\mathrm{miss}}$ reconstruction and a specific systematic uncertainty must be evaluated. This section discusses this uncertainty in the context of the track based soft term and the additional track $E_{\mathrm{T}}^{\mathrm{miss}}$ systematics.

10.1 TST systematics for EMTopo $E_{\mathrm{T}}^{\mathrm{miss}}$

The uncertainty on the soft term is characterised by how well it is modeled in simulation. In an event topology with zero true $E_{\mathrm{T}}^{\mathrm{miss}}$, the soft term momentum $p_{\mathrm{T}}^{\mathrm{soft}}$ is expected to be perfectly balanced against $p_{\mathrm{T}}^{\mathrm{hard}}$. Detector resolution effects spoil the equality between $p_{\mathrm{T}}^{\mathrm{hard}}$ and $p_{\mathrm{T}}^{\mathrm{soft}}$. Different projections of $p_{\mathrm{T}}^{\mathrm{soft}}$ along $p_{\mathrm{T}}^{\mathrm{hard}}$ in data and MC can be used to study the modelling of the soft term. Three projected quantities illustrated in Figure 4 are studied:

- **The parallel scale (Δ_L)**, representing the mean value of the parallel projection of $p_{\mathrm{T}}^{\mathrm{soft}}$ along $p_{\mathrm{T}}^{\mathrm{hard}}$. The component from the projection is labelled $p_{\parallel}^{\mathrm{soft}}$.
- **The parallel resolution ($\sigma_{\parallel}$)**, defined as the root-mean-square (RMS) of $p_{\parallel}^{\mathrm{soft}}$.
- **The transverse resolution ($\sigma_{\perp}$)**, defined as the root-mean-square (RMS) of the perpendicular component of $p_{\mathrm{T}}^{\mathrm{soft}}$ with respect to $p_{\mathrm{T}}^{\mathrm{hard}}$. The component from the projection is labelled $p_{\perp}^{\mathrm{soft}}$.

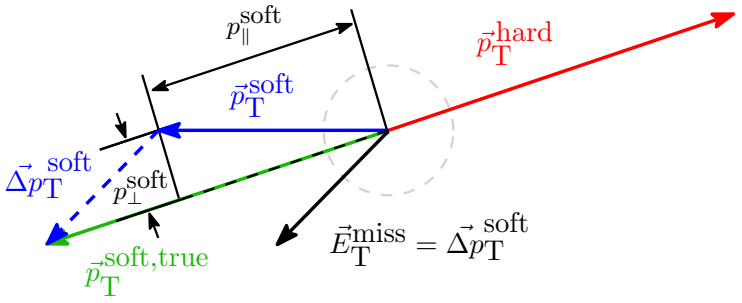

Figure 4: Sketch of the track-based soft term projections with respect to $p_{\mathrm{T}}^{\mathrm{hard}}$ for the calculation of the TST systematic uncertainties.

The transverse scale is not of physical interest as it is consistent with zero in data and simulation as found in Reference [3].

The systematic uncertainty is computed from the maximal disagreement between the 2015+2016 data with respect to different Monte Carlo generator plus parton shower models for a certain set of $p_{\mathrm{T}}^{\mathrm{hard}}$ bins. To account for any differences between event topologies with large numbers of jets and those without any jets, the total systematic is additionally split into jet-inclusive and jet-veto selections and merged later as the maximal variation of these two cases. In addition the fast detector simulation, called ATLFAST2 [53, 54], does not require any additional systematic uncertainties and is labelled AFII. Figure 5 shows the three projected quantities for the jet-inclusive and jet-veto cases. The resulting systematic envelope (see Table 3) is shown centered on data, and by construction, all the considered Monte Carlo generators plus parton shower models are covered by this systematic envelope. The resolutions in simulation are typically smaller than that observed in data as seen in Figure 5.

To apply the systematic uncertainties from Table 3, the projection of the soft term is smeared by a Gaussian of the width corresponding to its $p_{\mathrm{T}}^{\mathrm{hard}}$ value for the resolution uncertainties. The scale variation adds the value corresponding to its $p_{\mathrm{T}}^{\mathrm{hard}}$ to the $p_{\parallel}^{\mathrm{soft}}$ and it is subtracted for the opposite variation.

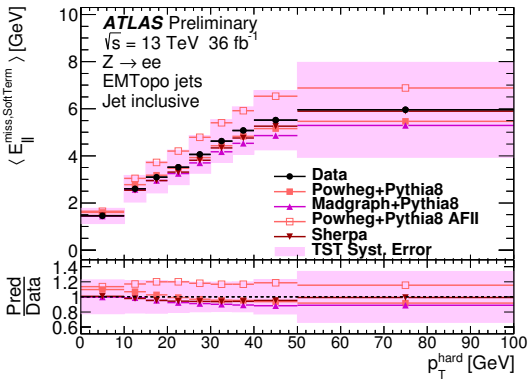

(a) Parallel scale, jet inclusive selection

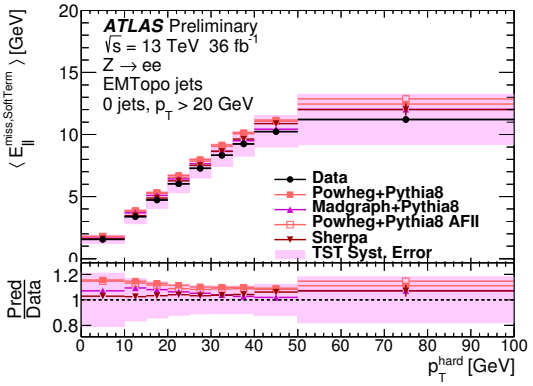

(b) Parallel scale, jet veto selection

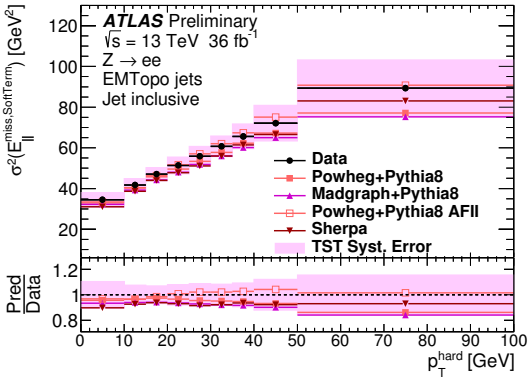

(c) Parallel resolution squared, jet inclusive selection

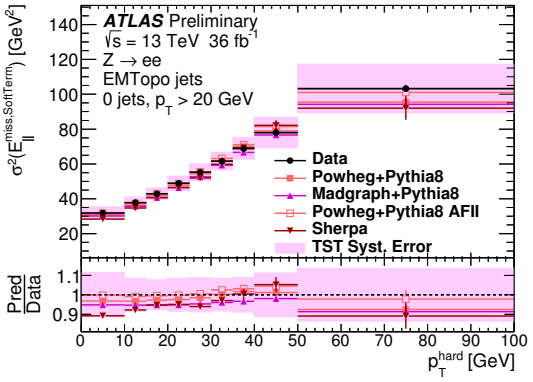

(d) Parallel resolution squared, jet veto selection

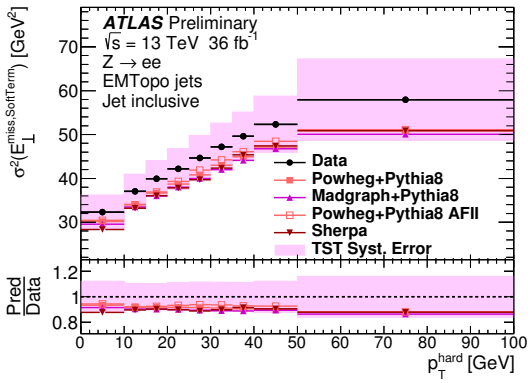

(e) Transverse resolution squared, jet inclusive selection

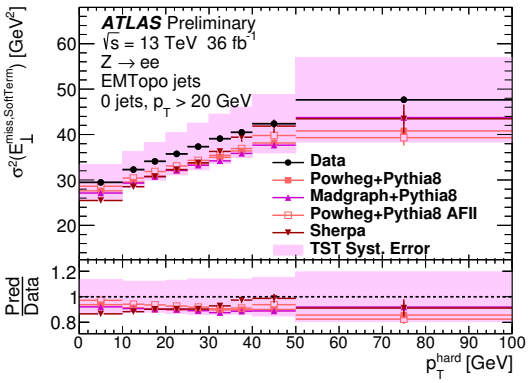

(f) Transverse resolution squared, jet veto selection

Figure 5: Parallel scale, parallel and transverse resolution plots for the track based soft term (TST). The pink band represents the resulting systematic uncertainty applied to the $Z \rightarrow ee$ Monte Carlo simulation. It is shown centered on data.

$p_{\mathrm{T}}^{\mathrm{hard}}$ bin [GeV]	$\sigma_{\parallel}$[GeV]	$\sigma_{\perp}$[GeV]	Δ_L[GeV]
0-10	1.87	2.00	0.25
10-15	1.77	1.97	0.50
15-20	1.73	1.98	0.63
20-25	1.91	2.09	0.71
25-30	2.20	2.24	0.75
30-35	2.21	2.29	0.85
35-40	2.36	2.36	0.96
40-50	2.69	2.38	1.07
50-200	3.71	3.04	1.96

Table 3: TST systematic envelope computed as the maximal differences between data and Monte Carlo samples for the parallel scale Δ_L, parallel and transverse resolutions $\sigma_{\parallel}, \sigma_{\perp}$.

10.2 TST systematics for PFlow $E_{\mathrm{T}}^{\mathrm{miss}}$

In analogy to the EMTopo $E_{\mathrm{T}}^{\mathrm{miss}}$, the TST systematics of Particle Flow $E_{\mathrm{T}}^{\mathrm{miss}}$ are computed following the same procedure described in Section 10.1. The validation plots obtained from the application of the Particle Flow systematic envelope (Table 4) to the Monte Carlo simulation samples are shown on Figure 6 for the various soft term projections. Because EMTopo-based and the Particle Flow-based TST have very similar definitions, the good agreement observed between the two systematic envelopes is expected.

$p_{\mathrm{T}}^{\mathrm{hard}}$ bin [GeV]	$\sigma_{\parallel}$[GeV]	$\sigma_{\perp}$[GeV]	Δ_L[GeV]
0-10	1.80	1.92	0.21
10-15	1.82	1.89	0.44
15-20	1.80	1.85	0.51
20-25	2.01	1.96	0.62
25-30	2.30	2.11	0.83
30-35	2.59	2.29	0.97
35-40	2.80	2.27	1.12
40-50	3.23	2.46	1.35
50-200	4.68	2.81	2.07

Table 4: PFlow TST systematic envelope computed as the maximal differences between data and Monte Carlo samples for the parallel scale Δ_L, parallel and perpendicular resolutions $\sigma_{\parallel}, \sigma_{\perp}$.

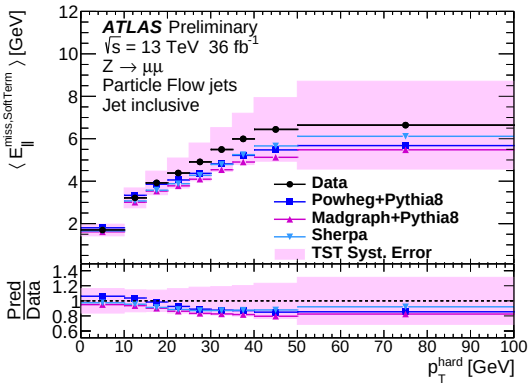

(a) Parallel scale, jet inclusive selection

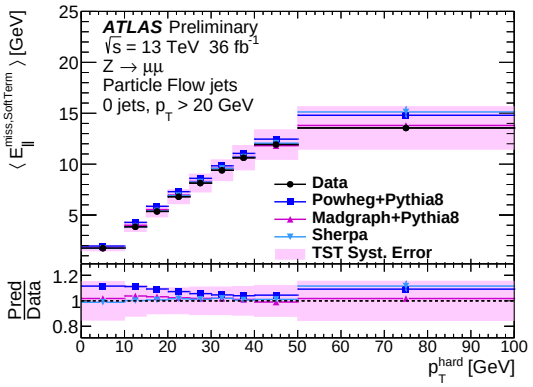

(b) Parallel scale, jet veto selection

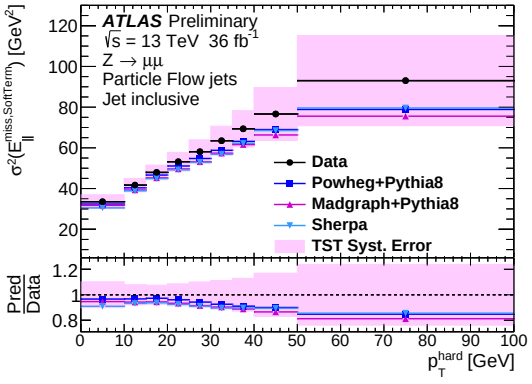

(c) Parallel resolution squared, jet inclusive selection

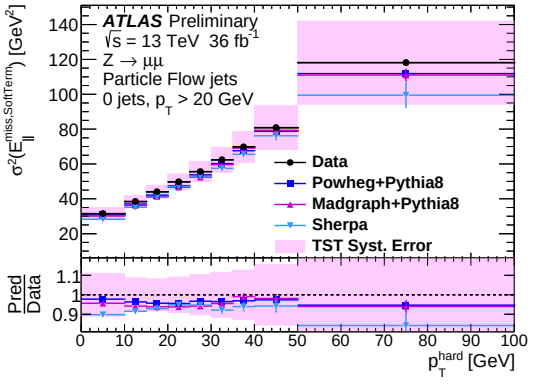

(d) Parallel resolution squared, jet veto selection

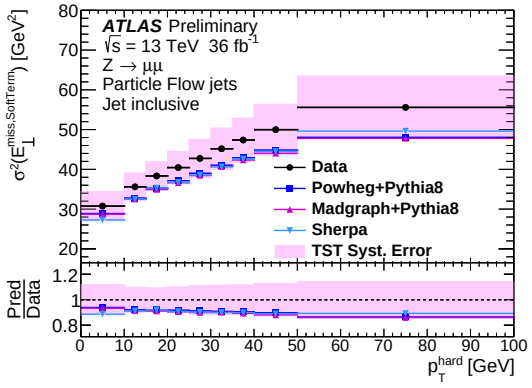

(e) Transverse resolution squared, jet inclusive selection

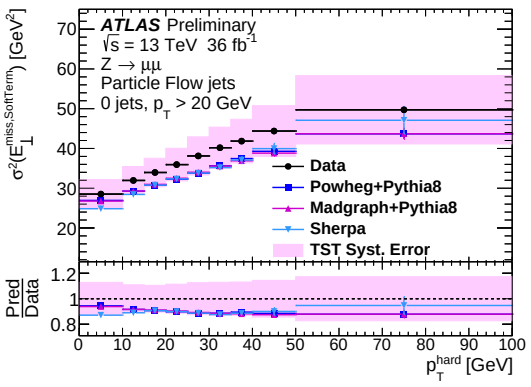

(f) Transverse resolution squared, jet veto selection

Figure 6: Parallel scale, parallel and transverse resolution plots for the Particle Flow track based soft term (PFlow TST). The pink band represents the resulting systematic uncertainty applied to the $Z \rightarrow \mu\mu$ Monte Carlo simulation. It is shown centered on data.

11 Modelling and performance of $E_{\mathrm{T}}^{\mathrm{miss}}$

In this section, the modelling of the $E_{\mathrm{T}}^{\mathrm{miss}}$ distributions is shown in a $Z \to \ell\ell$ selection by comparing simulation to data, and comparisons between the EMTopo and PFlow $E_{\mathrm{T}}^{\mathrm{miss}}$ definitions are made. In addition, the $E_{\mathrm{T}}^{\mathrm{miss}}$ resolution versus the number of pileup interactions per proton bunch crossing as well as an estimation of the $E_{\mathrm{T}}^{\mathrm{miss}}$ scale are shown.

11.1 Modelling of $E_{\mathrm{T}}^{\mathrm{miss}}$

In this section, basic $E_{\mathrm{T}}^{\mathrm{miss}}$ distributions are shown in a $Z \to \ell\ell$ selection in both data and simulation. All distributions in this section include the dominant systematic uncertainties on the high-p_{T} objects, the soft $E_{\mathrm{T}}^{\mathrm{miss}}$ term (described in Section 10) and pileup modelling [55]. These are the largest systematic uncertainties in the $E_{\mathrm{T}}^{\mathrm{miss}}$ for Z samples. The combined jet energy scale (JES) and η-intercalibration systematic uncertainties [47] are the largest contribution to the systematic uncertainty band, and their contribution to the total is shown separately.

The distributions of the EMTopo $E_{\mathrm{T}}^{\mathrm{miss}}$ are shown in data and simulation for $Z \to ee$ and $Z \to \mu\mu$ event selections in Figure 7. The PFlow $E_{\mathrm{T}}^{\mathrm{miss}}$ distributions are similarly shown in Figure 8. After normalisation of the simulated distributions with the generator cross-sections, the agreement between data and simulation is generally within the assigned systematic uncertainties for both $Z \to ee$ and $Z \to \mu\mu$ event topologies.

In both Figures 7 and 8, the JES uncertainty is large, and the agreement between data and simulation is degraded near $E_{\mathrm{T}}^{\mathrm{miss}}$ of around 100 GeV. The JVT threshold requirement is applied only for jets with both p_{T} below 60 GeV and $|\eta| < 2.4$. This allows pileup jets with $p_{\mathrm{T}} < 60$ GeV to be added into the $E_{\mathrm{T}}^{\mathrm{miss}}$ if the JES systematic variations push their p_{T} above the 60 GeV p_{T} threshold requirement.

The distribution of the track-based soft term is shown for the $Z \to ee$ and $Z \to \mu\mu$ event selections in EMTopo $E_{\mathrm{T}}^{\mathrm{miss}}$ in Figure 9. The dominant systematic uncertainty bands come from generator differences in the modelling of the underlying event as discussed in Section 10, and this systematic uncertainty on the $E_{\mathrm{T}}^{\mathrm{miss}}$ soft term is shown separately to indicate its shape and contribution size. The $Z \to ee$ and $Z \to \mu\mu$ event topologies have similar levels of agreement between data and simulation.

11.2 Comparisons of EMTopo and PFlow $E_{\mathrm{T}}^{\mathrm{miss}}$ distributions

The EMTopo and PFlow $E_{\mathrm{T}}^{\mathrm{miss}}$ distributions are compared in $Z \to \mu\mu$ simulation in Figure 10 for different jet selections. For the inclusive jet selection, the PFlow $E_{\mathrm{T}}^{\mathrm{miss}}$ has a slightly narrower distribution. The differences are much larger in the selection with no jets with $|\eta| > 2.4$ because the reconstruction differs more dramatically for jets with $|\eta| < 2.4$. The PFlow $E_{\mathrm{T}}^{\mathrm{miss}}$ has around half of the number of events at $E_{\mathrm{T}}^{\mathrm{miss}} = 100$ GeV. These performance improvements are attributed to the superior pileup mitigation of central PFlow jets, especially for jets p_{T} larger than 60 GeV where no vertex association is applied for EMTopo jets. Lastly, the 0-jet selection leads to a very similar distribution between EMTopo and PFlow $E_{\mathrm{T}}^{\mathrm{miss}}$. The PFlow $E_{\mathrm{T}}^{\mathrm{miss}}$ distribution has more 0-jet selection events because pileup rejection is better with PFlow jets. Jet efficiency improves for PFlow jets below around 40 GeV. At lower jet p_{T}, the EMTopo jets have worse pileup rejection. Small differences (of at most 10%) between the different $E_{\mathrm{T}}^{\mathrm{miss}}$ definitions are observed because of differences in event selection. The tail of the $E_{\mathrm{T}}^{\mathrm{miss}}$ distribution is mostly due

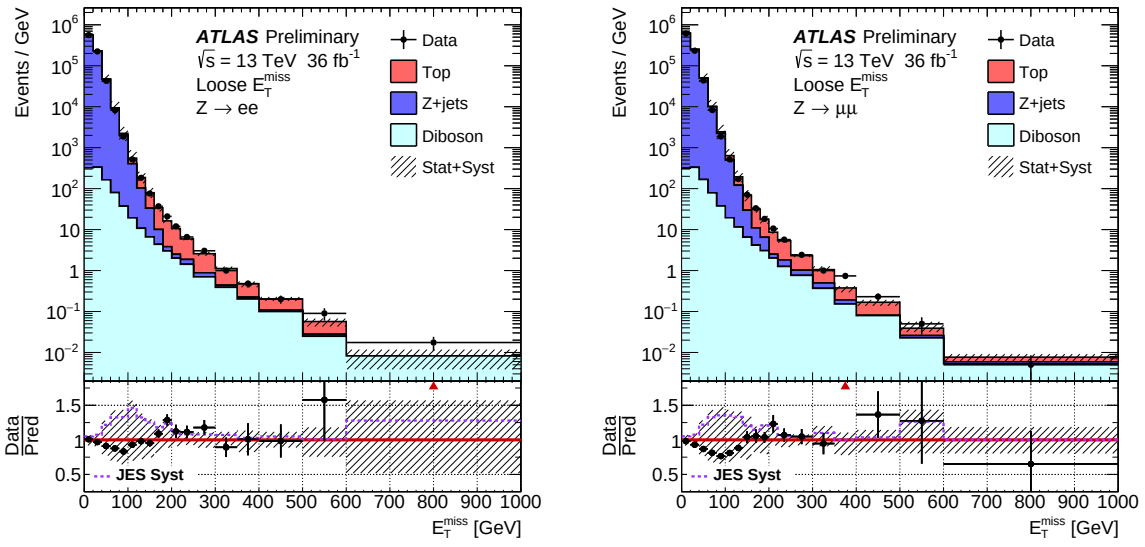

(a) (b)

Figure 7: Distributions of the EMTopo $E_{\mathrm{T}}^{\mathrm{miss}}$ using the Loose $E_{\mathrm{T}}^{\mathrm{miss}}$ operating point are shown in data and MC simulation for events satisfying the (a) $Z \rightarrow ee$ and (b) $Z \rightarrow \mu\mu$ selections. The lower panel of the figures shows the ratio of data to MC simulation, and the bands correspond to the combined systematic and MC statistical uncertainties. The largest contribution to the systematic uncertainty band comes from the combination of the jet energy scale (JES) and η-intercalibration systematic uncertainties, and it is shown in a dotted line. The far right bin includes the integral of all events with $E_{\mathrm{T}}^{\mathrm{miss}}$ above 600 GeV.

to muon mismeasurement or jets misidentified as electrons. This effect is effectively independent of jet reconstruction algorithm.

11.3 Resolution of $E_{\mathrm{T}}^{\mathrm{miss}}$

The resolution, as defined in Section 5.1, for the $E_{\mathrm{T}}^{\mathrm{miss}}$ is presented for the $Z \rightarrow \mu\mu$ event topology in Figure 11 as function of the number of reconstructed primary vertices in the event. The vertical error bands indicate the hard object uncertainties and the soft term systematic uncertainties discussed in Section 10 added in quadrature. For data, the error bars indicate the statistical uncertainty on the RMS. The data and simulation agree across the full range of N_{PV} and average interactions per proton bunch crossing $\langle\mu\rangle$. The $E_{\mathrm{T}}^{\mathrm{miss}}$ resolution increases roughly linearly at approximately 0.24 (0.13) GeV/$\langle\mu\rangle$ for the Loose (Tight) $E_{\mathrm{T}}^{\mathrm{miss}}$ operating point. The increasing amount of pileup activity degrades the $E_{\mathrm{T}}^{\mathrm{miss}}$ resolution from around 12 GeV at $N_{\mathrm{PV}} = 1$ to around 22 GeV at $N_{\mathrm{PV}} = 30$ for the Loose $E_{\mathrm{T}}^{\mathrm{miss}}$ operating point in Figure 11(b). The Tight $E_{\mathrm{T}}^{\mathrm{miss}}$ operating point in Figure 11(d) has a smaller degradation from around 12 GeV at $N_{\mathrm{PV}} = 1$ to around 18 GeV at $N_{\mathrm{PV}} = 30$. Deviations from linearity for the resolution a function of N_{PV} are due to an increase in vertex merging as pileup increases [56]. The PFlow $E_{\mathrm{T}}^{\mathrm{miss}}$ improves the $E_{\mathrm{T}}^{\mathrm{miss}}$ resolution consistently across the full range of N_{PV}.

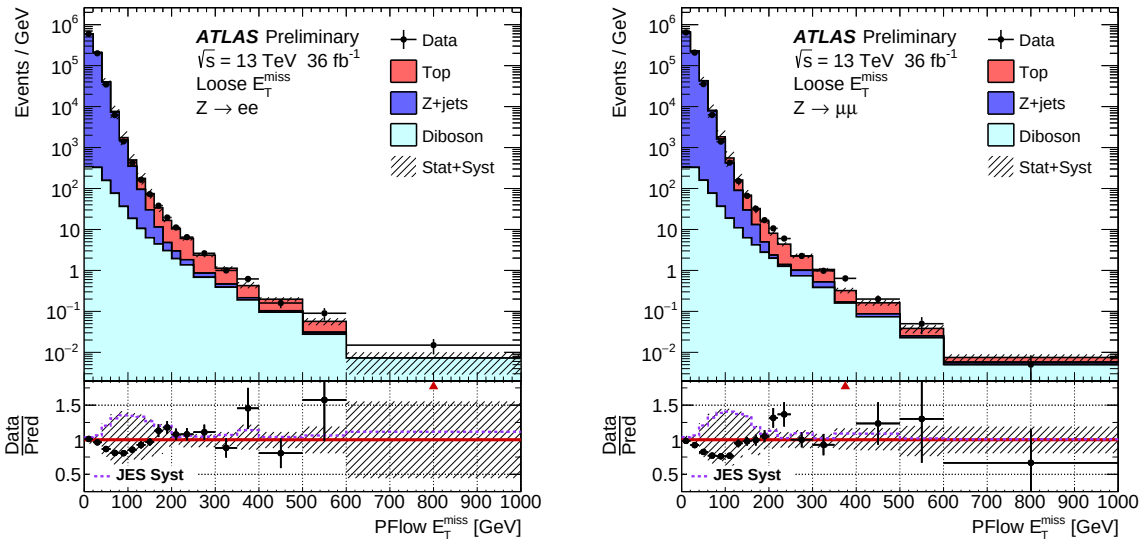

(a) (b)

Figure 8: Distributions of the PFlow $E_{\mathrm{T}}^{\mathrm{miss}}$ using the Loose $E_{\mathrm{T}}^{\mathrm{miss}}$ operating point are shown in data and MC simulation for events satisfying the (a) $Z \rightarrow ee$ and (b) $Z \rightarrow \mu\mu$ selections. The lower panel of the figures shows the ratio of data to MC simulation, and the bands correspond to the combined systematic and MC statistical uncertainties. The largest contribution to the systematic uncertainty band comes from the jet energy scale (JES) systematic uncertainties, and it is shown in a dotted line. The far right bin includes the integral of all events with $E_{\mathrm{T}}^{\mathrm{miss}}$ above 600 GeV.

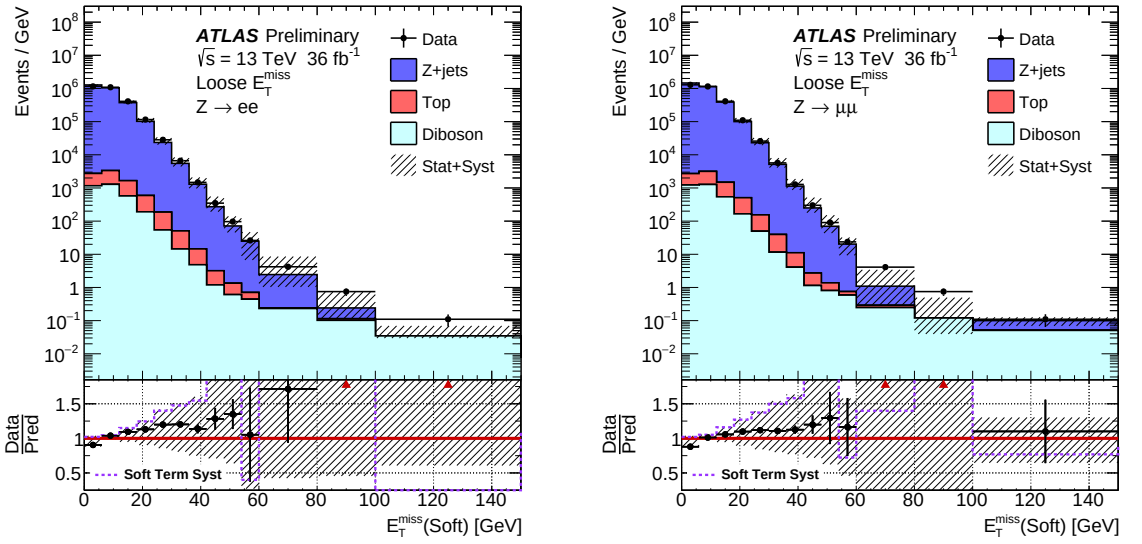

(a) (b)

Figure 9: Distributions of the EMTopo $E_{\mathrm{T}}^{\mathrm{miss}}$ using the Loose $E_{\mathrm{T}}^{\mathrm{miss}}$ operating point soft term are shown in data and MC simulation for events satisfying the (a) $Z \rightarrow ee$ and (b) $Z \rightarrow \mu\mu$ selections. The lower panel of the figures shows the ratio of data to MC simulation, and the bands correspond to the combined systematic and MC statistical uncertainties. The largest contribution to the systematic uncertainty band comes from the soft term systematics, and it is shown in a dotted line. The far right bin includes the integral of all events with soft $E_{\mathrm{T}}^{\mathrm{miss}}$ above 150 GeV.

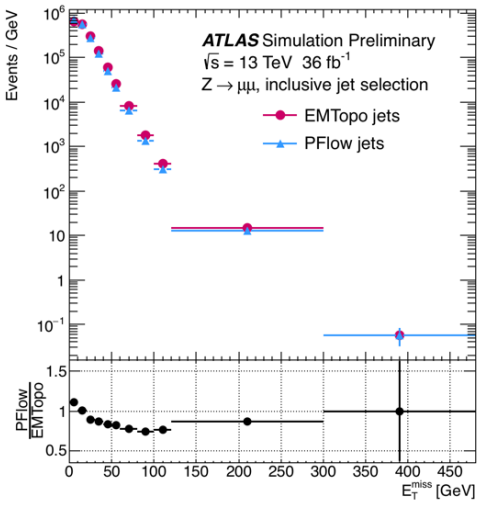

(a)

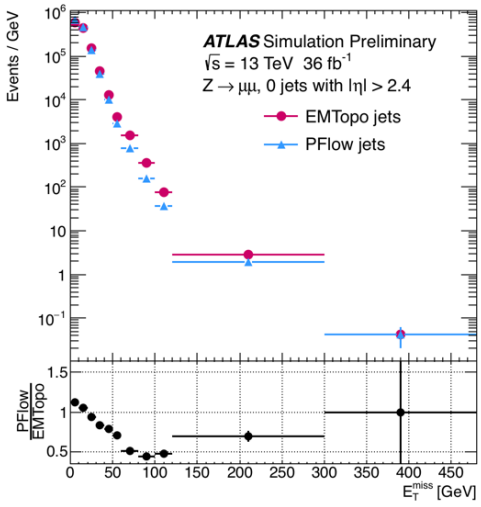

(b)

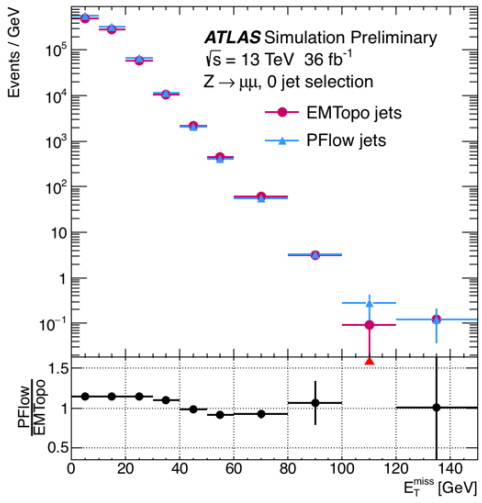

(c)

Figure 10: Distributions of the EMTopo and PFlow $E_{\mathrm{T}}^{\mathrm{miss}}$ using the Loose $E_{\mathrm{T}}^{\mathrm{miss}}$ operating point are shown in $Z \rightarrow \mu\mu$ simulation with the $Z \rightarrow \mu\mu$ event selection. The (a) inclusive, (b) no forward jet, and (c) 0-jet event selections are shown. The lower panel of the figures shows the ratio of PFlow to EMTopo $E_{\mathrm{T}}^{\mathrm{miss}}$ distributions. The far right bin includes the integral of all events with $E_{\mathrm{T}}^{\mathrm{miss}}$ above 120 GeV.

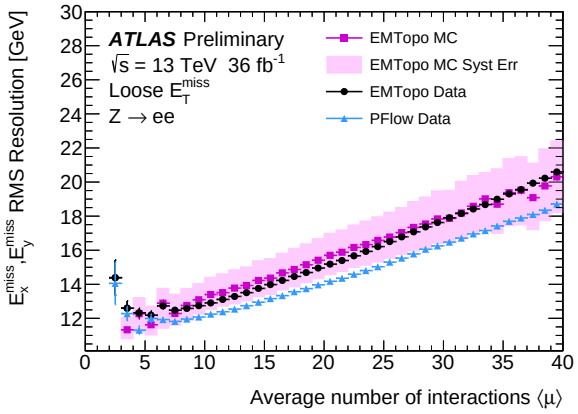

(a) Loose $E_{\mathrm{T}}^{\mathrm{miss}}$ resolution as a function of $\langle\mu\rangle$.

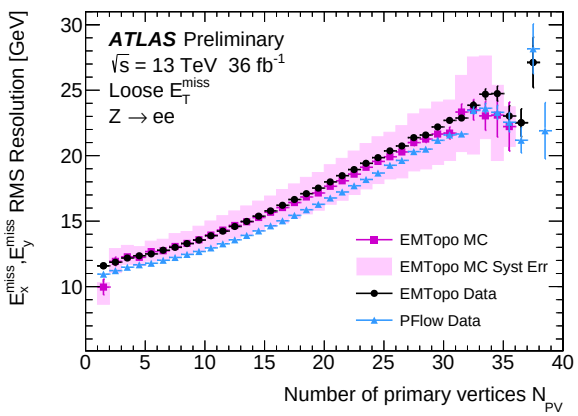

(b) Loose $E_{\mathrm{T}}^{\mathrm{miss}}$ resolution as a function of N_{PV}.

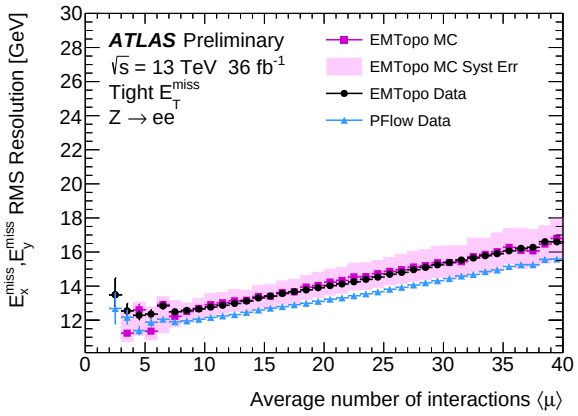

(c) Tight $E_{\mathrm{T}}^{\mathrm{miss}}$ resolution as a function of $\langle\mu\rangle$.

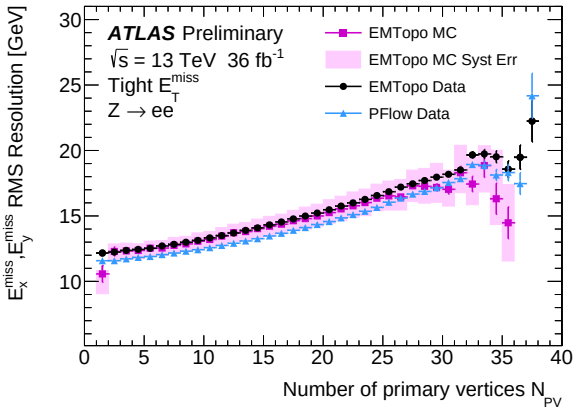

(d) Tight $E_{\mathrm{T}}^{\mathrm{miss}}$ resolution as a function of N_{PV}.

Figure 11: The RMS obtained from the combined distributions of EMTopo $E_{\mathrm{x}}^{\mathrm{miss}}$ and $E_{\mathrm{y}}^{\mathrm{miss}}$ using the Loose $E_{\mathrm{T}}^{\mathrm{miss}}$ operating point for data with EMTopo jets (circular marker) and PFlow jets (triangular marker) and MC simulation with EMTopo jets (square marker) in a $Z \rightarrow ee$ event selection are shown versus (a) $\langle\mu\rangle$ and (b) N_{PV}. The same distributions for the Tight $E_{\mathrm{T}}^{\mathrm{miss}}$ working point are shown in (c) and (d), respectively. The small non-Z backgrounds are included in the simulation. The pink band indicates the size of the detector level systematic uncertainties. The performance of PFlow $E_{\mathrm{T}}^{\mathrm{miss}}$ in data is also shown in blue.

11.4 Measuring $E_{\mathrm{T}}^{\mathrm{miss}}$ recoil versus p_{T}^{Z}

In events with $Z \rightarrow ee$ decays, the $\vec{p_{\mathrm{T}}}$ of the Z boson defines an axis in the transverse plane of the ATLAS detector, and for events with 0-jets, the $\vec{E}_{\mathrm{T}}^{\mathrm{miss}}$ should balance the $\vec{p_{\mathrm{T}}}$ of the Z boson ($\vec{p}_{\mathrm{T}}^{Z}$) along this axis. The component of the $\vec{E}_{\mathrm{T}}^{\mathrm{miss}}$ along the $\vec{p}_{\mathrm{T}}^{Z}$ axis is sensitive to biases in detector responses [57]. The unit vector of $\vec{p}_{\mathrm{T}}^{Z}$ is labelled as $\hat{\mathcal{A}}_Z$ and is defined as:

$$\hat{\mathcal{A}}_Z = \frac{\vec{p_{\mathrm{T}}}^{\ell^+} + \vec{p_{\mathrm{T}}}^{\ell^-}}{|\vec{p_{\mathrm{T}}}^{\ell^+} + \vec{p_{\mathrm{T}}}^{\ell^-}|}, \tag{6}$$

where $\vec{p_{\mathrm{T}}}^{\ell^+}$ and $\vec{p_{\mathrm{T}}}^{\ell^-}$ are the transverse momentum vectors of the leptons from the Z boson decay.

The average of the $\vec{E}_{\mathrm{T}}^{\mathrm{miss}}$ projected in $\hat{\mathcal{A}}_Z$ direction is labelled as $\langle \vec{E}_{\mathrm{T}}^{\mathrm{miss}} \cdot \hat{\mathcal{A}}_Z \rangle$. In principle this quantity should be zero for all p_{T}^{Z}. However, the calibration of p_{T}^{Z} and lack of calibration of the soft terms means that any differences are mostly due to miscalibrations of the $E_{\mathrm{T}}^{\mathrm{miss}}$. The $\langle \vec{E}_{\mathrm{T}}^{\mathrm{miss}} \cdot \hat{\mathcal{A}}_Z \rangle$ is shown versus p_{T}^{Z} in Figure 12 for EMTopo $E_{\mathrm{T}}^{\mathrm{miss}}$ in data and MC simulation. The hashed band indicates the size of the systematic uncertainties. For $p_{\mathrm{T}}^{Z} > 20$ GeV, the $\langle \vec{E}_{\mathrm{T}}^{\mathrm{miss}} \cdot \hat{\mathcal{A}}_Z \rangle$ returns toward zero as the jet terms start to dominate over the soft term, which is most relevant at lower p_{T}^{Z}. The scale of the track-based soft term is not perfect due to the missing neutral particles. The data and MC simulation agree within the assigned systematic uncertainties. While the $\langle \vec{E}_{\mathrm{T}}^{\mathrm{miss}} \cdot \hat{\mathcal{A}}_Z \rangle$ plateaus between -4 and -6 GeV, the systematic band covers the differences with zero above 200 GeV in p_{T}^{Z}.

The Tight $E_{\mathrm{T}}^{\mathrm{miss}}$ working point, which raises for the jet p_{T} threshold from 20 GeV to 30 GeV for $|\eta| > 2.4$ has around 1 GeV lower $\langle \vec{E}_{\mathrm{T}}^{\mathrm{miss}} \cdot \hat{\mathcal{A}}_Z \rangle$ for p_{T}^{Z} larger than 100 GeV. The fJVT $E_{\mathrm{T}}^{\mathrm{miss}}$ working point lies between the Loose and Tight $E_{\mathrm{T}}^{\mathrm{miss}}$ working points.

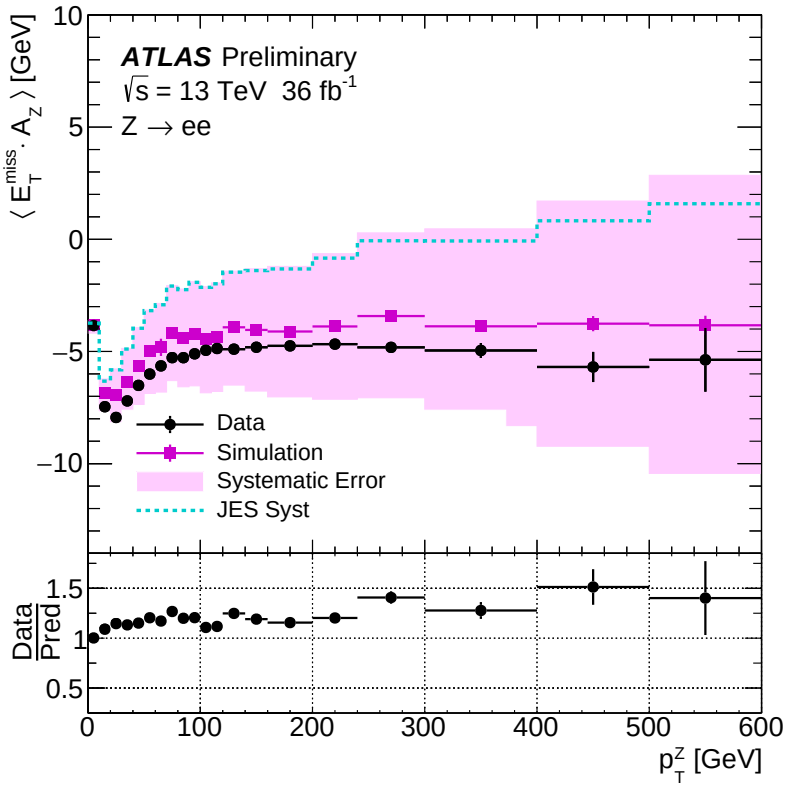

(a)

Figure 12: The average $E_{\mathrm{T}}^{\mathrm{miss}}$ projected onto $\hat{\mathcal{A}}_Z$ for EMTopo $E_{\mathrm{T}}^{\mathrm{miss}}$ is shown versus p_{T}^Z in data (circular marker) and MC simulation (square marker). The Loose $E_{\mathrm{T}}^{\mathrm{miss}}$ working point is used, and the small non-Z backgrounds are included in the simulation. The pink band indicates the size of the detector level systematic uncertainties, which also cover variations associated with eta dependence and pileup. The largest individual systematic uncertainty comes from the jet energy scale (JES). The size of the band reflects the sensitivity of the $E_{\mathrm{T}}^{\mathrm{miss}}$ projection to variations in object calibration, as a small uncertainty can result in a large offset for large p_{T}^Z. At low p_{T}^Z the $\langle \vec{E}_{\mathrm{T}}^{\mathrm{miss}} \cdot \hat{\mathcal{A}}_Z \rangle$ is much less than zero because the $E_{\mathrm{T}}^{\mathrm{miss}}$ is mostly represented by the TST, which does not capture the neutral energy. As p_{T}^Z increases more of the hadronic recoil is reconstructed as calibrated hard objects and $\langle \vec{E}_{\mathrm{T}}^{\mathrm{miss}} \cdot \hat{\mathcal{A}}_Z \rangle$ recovers toward zero.

12 Conclusion

The object-based $E_{\mathrm{T}}^{\mathrm{miss}}$ reconstruction in ATLAS is used in a large number of physics analyses to reject backgrounds without real $E_{\mathrm{T}}^{\mathrm{miss}}$, estimate missing neutrino transverse momentum, and search for new invisible particles. This note presents the performance of the $E_{\mathrm{T}}^{\mathrm{miss}}$ reconstruction evaluated with proton–proton LHC collision data acquired in 2015 and 2016 with the ATLAS detector at $\sqrt{s} = 13$ TeV and corresponding to $36\,\mathrm{fb}^{-1}$.

The $E_{\mathrm{T}}^{\mathrm{miss}}$ performance is studied using two different jet definitions as inputs to the $E_{\mathrm{T}}^{\mathrm{miss}}$ reconstruction: EMTopo and PFlow jets. This note presents the first study of $E_{\mathrm{T}}^{\mathrm{miss}}$ built with PFlow jets. A degradation of the $E_{\mathrm{T}}^{\mathrm{miss}}$ resolution is observed for increasing $\langle\mu\rangle$ and N_{PV} due to pileup and detector resolution effects, regardless of input jet collection. However, PFlow $E_{\mathrm{T}}^{\mathrm{miss}}$ shows less degradation for increasing pileup compared to EMTopo $E_{\mathrm{T}}^{\mathrm{miss}}$. Additional performance measurements considered in these studies include the estimate of tails in the $E_{\mathrm{T}}^{\mathrm{miss}}$ distribution. PFlow $E_{\mathrm{T}}^{\mathrm{miss}}$ distributions show smaller tails, reflecting a lower sensitivity to residual pileup entering the jet contribution to $E_{\mathrm{T}}^{\mathrm{miss}}$.

Different $E_{\mathrm{T}}^{\mathrm{miss}}$ object selection and jet reconstruction techniques were studied and their impact on $E_{\mathrm{T}}^{\mathrm{miss}}$ performance evaluated. Reducing the number of low-p_{T} forward jets included in the $E_{\mathrm{T}}^{\mathrm{miss}}$ reconstruction markedly improves the $E_{\mathrm{T}}^{\mathrm{miss}}$ resolution dependence on pileup. A new technique for resolving electron-jet overlap reduces the amount of fake $E_{\mathrm{T}}^{\mathrm{miss}}$ in the tails, and a new jet cleaning definition removes events with fake jets from the $E_{\mathrm{T}}^{\mathrm{miss}}$ input.

The systematic uncertainty contribution from the soft event to the reconstructed $E_{\mathrm{T}}^{\mathrm{miss}}$ is determined with $Z \to \mu\mu$ and $Z \to ee$ final states with and without jets. The MC simulation tends to underestimate the perpendicular resolution and overestimate the scale and parallel resolution, in each case differing from data by at most 20%. The performance evaluation of $E_{\mathrm{T}}^{\mathrm{miss}}$ response and resolution for the inclusive $Z \to \mu\mu$ sample shows that data and MC simulations agree within the assigned systematic uncertainties.

The many improvements and new definitions documented in this note offer ATLAS analyses new $E_{\mathrm{T}}^{\mathrm{miss}}$ definitions and a wide array of configurations and working points for various analysis needs. Refined signal ambiguity resolution, better performance at higher pileup, and reduced fake $E_{\mathrm{T}}^{\mathrm{miss}}$ all have the potential to improve searches for new physics and Standard Model measurements across the ATLAS physics program.

References

[1] ATLAS Collaboration, *The ATLAS Experiment at the CERN Large Hadron Collider*, JINST **3** (2008) S08003.

[2] ATLAS Collaboration, *Performance of missing transverse momentum reconstruction in proton–proton collisions at $\sqrt{s}$ = 7 TeV with ATLAS*, Eur. Phys. J. C **72** (2012) 1844, arXiv: 1108.5602 [hep-ex].

[3] ATLAS Collaboration, *Performance of algorithms that reconstruct missing transverse momentum in $\sqrt{s}$ = 8 TeV proton–proton collisions in the ATLAS detector*, Eur. Phys. J. C **77** (2017) 241, arXiv: 1609.09324 [hep-ex].

[4] ATLAS Collaboration, *Performance of missing transverse momentum reconstruction with the ATLAS detector using proton-proton collisions at $\sqrt{s}$ = 13 TeV*, (2018), arXiv: 1802.08168 [hep-ex].

[5] ATLAS Collaboration, *Jet reconstruction and performance using particle flow with the ATLAS Detector*, Eur. Phys. J. C **77** (2017) 466, arXiv: 1703.10485 [hep-ex].

[6] ATLAS Collaboration, *ATLAS Insertable B-Layer Technical Design Report*, tech. rep. CERN-LHCC-2010-013. ATLAS-TDR-19, 2010, URL: https://cds.cern.ch/record/1291633.

[7] ATLAS Collaboration, *Monitoring and data quality assessment of the ATLAS liquid argon calorimeter*, JINST **9** (2014) P07024, arXiv: 1405.3768 [hep-ex].

[8] ATLAS Collaboration, *Operation and performance of the ATLAS semiconductor tracker*, JINST **9** (2014) P08009, arXiv: 1404.7473 [hep-ex].

[9] ATLAS Collaboration, *Selection of jets produced in 13TeV proton-proton collisions with the ATLAS detector*, tech. rep. ATLAS-CONF-2015-029, CERN, 2015, URL: https://cds.cern.ch/record/2037702.

[10] ATLAS Collaboration, *The ATLAS Simulation Infrastructure*, Eur. Phys. J. C **70** (2010) 823, arXiv: 1005.4568 [physics.ins-det].

[11] T. Sjöstrand, S. Mrenna and P. Z. Skands, *A Brief Introduction to PYTHIA 8.1*, Comput. Phys. Commun. **178** (2008) 852, arXiv: 0710.3820 [hep-ph].

[12] ATLAS Collaboration, *Summary of ATLAS Pythia 8 tunes*, ATL-PHYS-PUB-2012-003, 2012, URL: https://cds.cern.ch/record/1474107.

[13] R. D. Ball et al., *Parton distributions for the LHC Run II*, JHEP **04** (2015) 040.

[14] T. Gleisberg et al., *Event generation with SHERPA 1.1*, JHEP **02** (2009) 007, arXiv: 0811.4622 [hep-ph].

[15] D. J. Lange, *The EvtGen particle decay simulation package*, Nucl. Instrum. Meth. A **462** (2001) 152.

[16] F. Cascioli, P. Maierhofer and S. Pozzorini, *Scattering Amplitudes with Open Loops*, Phys. Rev. Lett. **108** (2012) 111601, arXiv: 1111.5206 [hep-ph].

[17] T. Gleisberg and S. Höche, *Comix, a new matrix element generator*, JHEP **0812** (2008) 039, arXiv: 0808.3674 [hep-ph].

[18] S. Catani, L. Cieri, G. Ferrera, D. de Florian and M. Grazzini, *Vector boson production at hadron colliders: a fully exclusive QCD calculation at NNLO*, Phys. Rev. Lett. **103** (2009), arXiv: 0903.2120 [hep-ph].

[19] S. Schumann and F. Krauss, *A Parton shower algorithm based on Catani-Seymour dipole factorisation*, JHEP **0803** (2008) 038, arXiv: 0709.1027 [hep-ph].

[20] S. Höche, F. Krauss, M. Schönherr and F. Siegert, *QCD matrix elements + parton showers: The NLO case*, JHEP **04** (2013) 027, arXiv: 1207.5030 [hep-ph].

[21] S. Frixione, G. Ridolfi and P. Nason, *A Positive-weight next-to-leading-order Monte Carlo for heavy flavour hadroproduction*, JHEP **09** (2007) 126, arXiv: 0707.3088 [hep-ph].

[22] J. Alwall et al., *The automated computation of tree-level and next-to-leading order differential cross sections, and their matching to parton shower simulations*, JHEP **07** (2014) 079, arXiv: 1405.0301 [hep-ph].

[23] W. Lukas, *Fast Simulation for ATLAS: Atlfast-II and ISF*, tech. rep. ATL-SOFT-PROC-2012-065, CERN, 2012, URL: https://cds.cern.ch/record/1458503.

[24] N. Davidson, T. Przedzinski and Z. Was, *PHOTOS Interface in C++: Technical and Physics Documentation*, (2010), arXiv: 1011.0937 [hep-ph].

[25] H.-L. Lai, M. Guzzi, J. Huston, Z. Li, P. M. Nadolsky et al., *New parton distributions for collider physics*, Phys. Rev. D **82** (2010) 074024, arXiv: 1007.2241 [hep-ph].

[26] R. D. Ball et al., *Parton distributions with LHC data*, Nucl. Phys. B **867** (2013) 244, arXiv: 1207.1303 [hep-ph].

[27] ATLAS Collaboration, *Measurement of the Z/γ^* boson transverse momentum distribution in pp collisions at $\sqrt{s} = 7$ TeV with the ATLAS detector*, JHEP **09** (2014) 145, arXiv: 1406.3660 [hep-ex].

[28] ATLAS Collaboration, *ATLAS Pythia 8 tunes to 7 TeV data*, ATL-PHYS-PUB-2014-021, 2014, URL: https://cds.cern.ch/record/1966419.

[29] S. Alioli, P. Nason, C. Oleari and E. Re, *NLO single-top production matched with shower in POWHEG: s- and t-channel contributions*, JHEP **09** (2009) 111, [Erratum: JHEP02,011(2010)], arXiv: 0907.4076 [hep-ph].

[30] E. Re, *Single-top Wt-channel production matched with parton showers using the POWHEG method*, Eur. Phys. J. **C71** (2011) 1547, arXiv: 1009.2450 [hep-ph].

[31] M. Czakon, P. Fiedler and A. Mitov, *Total Top-Quark Pair-Production Cross Section at Hadron Colliders Through $O(\alpha_s^4)$*, Phys. Rev. Lett. **110** (2013) 252004, arXiv: 1303.6524 [hep-ph].

[32] M. Czakon and A. Mitov,
Top++: A Program for the Calculation of the Top-Pair Cross-Section at Hadron Colliders,
(2011), arXiv: 1112.5675 [hep-ph].

[33] N. Kidonakis, *NNLL resummation for s-channel single top quark production*,
Phys. Rev. D **81** (2010) 054028, arXiv: 1001.5034 [hep-ph].

[34] N. Kidonakis, *Next-to-next-to-leading-order collinear and soft gluon corrections for t-channel single top quark production*, Phys. Rev. D **83** (2011) 091503, arXiv: 1103.2792 [hep-ph].

[35] N. Kidonakis,
Two-loop soft anomalous dimensions for single top quark associated production with a W- or H-,
Phys. Rev. D **82** (2010) 054018, arXiv: 1005.4451 [hep-ph].

[36] T. Sjöstrand, S. Mrenna and P. Z. Skands, *PYTHIA 6.4 Physics and Manual*, JHEP **05** (2006) 026,
arXiv: hep-ph/0603175.

[37] P. K. Skands, *Tuning Monte Carlo generators: The Perugia tunes*, Phys. Rev. D **82** (2010) 074018,
arXiv: 1005.3457 [hep-ex].

[38] J. Pumplin et al.,
New generation of parton distributions with uncertainties from global QCD analysis,
JHEP **07** (2002) 012, arXiv: hep-ph/0201195 [hep-ph].

[39] ATLAS Collaboration,
Electron and photon energy calibration with the ATLAS detector using LHC Run 1 data,
Eur. Phys. J. C **74** (2014) 3071, arXiv: 1407.5063 [hep-ex].

[40] ATLAS Collaboration, *Measurement of the muon reconstruction performance of the ATLAS detector using 2011 and 2012 LHC proton–proton collision data*, Eur. Phys. J. C **74** (2014) 3130,
arXiv: 1407.3935 [hep-ex].

[41] ATLAS Collaboration, *Search for photonic signatures of gauge-mediated supersymmetry in 13 TeV pp collisions with the ATLAS detector*, (2018), arXiv: 1802.03158 [hep-ex].

[42] ATLAS Collaboration, *Search for top squarks decaying to tau sleptons in pp collisions at* $\sqrt{s} = 13$ *TeV with the ATLAS detector*, (2018), arXiv: 1803.10178 [hep-ex].

[43] ATLAS Collaboration, *Electron efficiency measurements with the ATLAS detector using the 2015 LHC proton–proton collision data*, ATLAS-CONF-2016-024, 2016,
URL: https://cds.cern.ch/record/2157687.

[44] *Electron and photon energy calibration with the ATLAS detector using data collected in 2015 at* $\sqrt{s} = 13$ TeV, tech. rep. ATL-PHYS-PUB-2016-015, CERN, 2016,
URL: https://cds.cern.ch/record/2203514.

[45] W. Lampl et al., *Calorimeter Clustering Algorithms: Description and Performance*,
ATL-LARG-PUB-2008-002, 2008, URL: https://cds.cern.ch/record/1099735.

[46] M. Cacciari, G. P. Salam and G. Soyez, *The Anti-k(t) jet clustering algorithm*,
JHEP **04** (2008) 063, arXiv: 0802.1189 [hep-ph].

[47] ATLAS Collaboration, *Jet energy scale measurements and their systematic uncertainties in proton–proton collisions at* $\sqrt{s} = 13$ *TeV with the ATLAS detector*,
Phys. Rev. D **96** (2017) 072002, arXiv: 1703.09665 [hep-ex].

[48] ATLAS Collaboration, *Performance of pile-up mitigation techniques for jets in pp collisions at $\sqrt{s}$ = 8 TeV using the ATLAS detector*, Eur. Phys. J. C **76** (2016) 581, arXiv: 1510.03823 [hep-ex].

[49] M. Cacciari, G. P. Salam and G. Soyez, *The Catchment Area of Jets*, JHEP **04** (2008) 005, arXiv: 0802.1188 [hep-ph].

[50] ATLAS Collaboration, *Identification and rejection of pile-up jets at high pseudorapidity with the ATLAS detector*, Eur. Phys. J. **77** (2017) 580.

[51] ATLAS Collaboration, *Electron efficiency measurements with the ATLAS detector using 2012 LHC proton–proton collision data*, Eur. Phys. J. **77** (2017) 195, arXiv: 1434-6052 [hep-ph].

[52] ATLAS Collaboration, *Forward Jet Vertex Tagging: A new technique for the identification and rejection of forward pileup jets*, ATL-PHYS-PUB-2015-034, 2015, URL: https://cds.cern.ch/record/2042098.

[53] ATLAS Collaboration, *The ATLAS Simulation Infrastructure*, Eur. Phys. J. **C70** (2010) 823, arXiv: 1005.4568 [physics.ins-det].

[54] ATLAS Collaboration, *The simulation principle and performance of the ATLAS fast calorimeter simulation FastCaloSim*, tech. rep. ATL-PHYS-PUB-2010-013, CERN, 2010, URL: https://cds.cern.ch/record/1300517.

[55] ATLAS Collaboration, *Performance of the ATLAS Inner Detector Track and Vertex Reconstruction in High Pile-Up LHC Environment*, ATLAS-CONF-2012-042, 2012, URL: https://cds.cern.ch/record/1435196.

[56] ATLAS Collaboration, *Vertex Reconstruction Performance of the ATLAS Detector at $\sqrt{s}$ = 13 TeV*, ATL-PHYS-PUB-2015-026, 2015, URL: https://cds.cern.ch/record/2037717.

[57] ATLAS Collaboration, *Expected Performance of the ATLAS Experiment - Detector, Trigger and Physics (Jet and E_T^{miss} chapter)*, (2008), arXiv: 0901.0512 [hep-ex].